Modeling of the Frequency Dependent Detective Quantum Efficiency of X-Ray Imaging Detectors

Md. Wasiur Rahman

A Thesis

In the Department

of

Electrical and Computer Engineering

Presented in Partial Fulfillment of the Requirements

for the Degree of Master of Applied Science at

Concordia University

Montréal Québec Canada

July 2010

Canada

ABSTRACT

Modeling of Frequency Dependent Detective Quantum Efficiency of X-ray Imaging Detectors

Md. Wasiur Rahman

Direct conversion flat panel x-ray imaging detector is presently one of the important tools in medical diagnosis of a patient. It provides an excellent image quality, portability, and dose utilization. Amorphous selenium based direct conversion detector with an active matrix array has been in the focus of researchers for the last two decades and extensive work and improvement have been done on this. There are several parameters of an x-ray imaging detector through which the imaging performance of a detector could be measured. The most important measure is the frequency, f, dependent detective quantum efficiency, DQE(f). In this thesis, we have proposed a parallel cascaded linear system model for calculating DQE(f) by considering the effects of K-fluorescence reabsorption, the range of primary photo electrons, charge carrier trapping, aperture function, noise aliasing, and addition of electronic noise. DQE (Detective Quantum Efficiency) depends significantly on the transport properties (mobility-lifetime product) and the creation of K-fluorescent x-ray photons. The DQE model is applied to fluoroscopic and mammographic detectors and is validated with the recent published experimental data. It has been found that the DQE(f) can be improved by ensuring that the carrier with the higher mobility-lifetime product is drifted towards the pixel electrode, i.e., the bottom electrode of the detector. A

simplified zero spatial frequency, DQE(0), is also proposed in this thesis. There exists an optimum detector thickness that maximizes the DQE under charge carrier trapping. Although the model is applied to Amorphous Selenium (a-Se) and Mercuric Iodide (HgI_2) based imaging detectors, it can also be applied to analyze the DQE(f) performance of the imaging detectors based on other photoconductive materials like CdZnTe, PbI_2 etc.

To my loving parents

&

lovely wife.

ACKNOWLEDGMENTS

TABLE OF CONTENTS

LIST OF FIGURES

LIST OF TABLES

LIST OF ABBREVIATIONS

a-Se   Amorphous Selenium

A/D   Analog to Digital

AMA   Active Matrix Array

AMFPI   Active Matrix Flat Panel Imager

DQE   Detective Quantum Efficiency

EHP   Electron Hole Pair

FET   Field Effect Transistor

keV   Kilo Electron Volt

kVp   Kilo Volt Peak

MeV   Mega Electron Volt

MRI   Magnetic Resonance Imaging

MTF   Modulation Transfer Function

NPS   Noise Power Spectrum

Poly-HgI$_2$ Polycrystalline HgI$_2$

TFT   Thin Film Transistor

CHAPTER 1 INTRODUCTION

1.1 Radiographic Imaging

Radiography is the method of viewing the inside of an object by using the x rays. An x-ray is a form of electromagnetic radiation and its wavelength is in the range of 10 to 0.01 nanometers. In 1895 Wilhem Conrad Rontgen first discovered x rays and 15 years later he got the Nobel prize for this invention. The discovery of x-ray has led very quickly to the development of radiology and medical imaging. Radiographic imaging is one of the most useful tools for the physicians in making a diagnosis of the patient. The basis of the radiographic imaging system is the differential attenuation of the ionizing radiation through different structures and tissues in the body [1]. Due to the several advantages to x-ray imaging, digital x-ray system has drawn much more interest now-a-days than that of film based analog technology. Image portability, improvement of image quality, and dose utilization are the most important advantages of the digital imaging.

The attenuation of the electromagnetic radiation is varied according to the different tissues and structures of the body of the patient on a cassette film in the analog system. Patients are positioned in between the x-ray generator and the detector. X rays pass through the patient's body with different attenuation in the different parts of the body and at the end, exposed to the detector. There is cassette film right behind the phosphor screen of the detector. When the x-ray exposure reaches to the screen, the

screen gives off the light which exposes the film and leaves the image. After the development of the film the image can be visible. This film based analog technology has some drawbacks like long exposure, inefficiency, and high x-ray dosage. In the digital radiography the cassette film is replaced by a digital image capture device in order to record the x-ray image.

1.2 Flat Panel Detector

A flat panel x-ray image detector is a large area integrated circuit by which an x-ray image can be captured and can be converted into digital form. A flat panel x ray imaging detector is replaced in a digital radiographic system instead of using cassette films in a conventional radiographic system. Flat panel detectors with active matrix arrays are called active matrix flat panel imagers (AMFPI). There are arrays of two dimensional pixels in a flat panel imager. Each of the pixels works as an individual detector. The pixel produces a certain amount of charge in respose to the amount of radiation it receives.

The AMFPI concept is depicted in Figure 1.1[2]. The conversion of x-ray photon to electric charges can be done by two most common approaches by using indirect conversion detector and direct conversion detector. Indirect conversion detector systems are based on thin film transistor arrays which are constructed by adding amorphous silicon photodiode circuitry and a scintillator as the top layers of the thin film transistor array. The absorbed x-ray photons are converted into visible light photons by the scintillator. Using the photodiode circuitry electronic charges are produced from the visible light photons. It can be said that each photodiode is representing each pixel. The

electric charges at each pixel are read out by the peripheral electronic circuitry. The resolution of the direct conversion detector is much better than that of the indirect conversion detector. In the following section direct conversion detector approach will be described.

Flat Panel X-Ray Image Detector
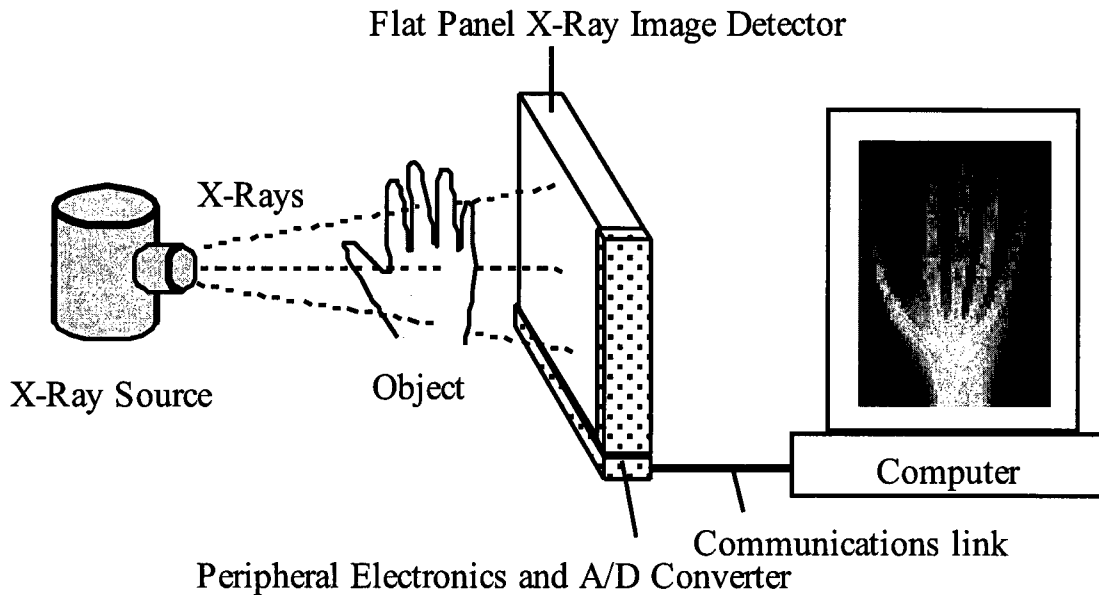
Figure 1.1 Schematic illustration of an AMFPI system [2].

1.3 Direct Conversion Detectors

Direct conversion detector systems are better in image quality to indirect conversion systems and also cheaper and easier to manufacture due to their simpler structure [6, 7]. Now-a-days the direct approach becomes major contending choice in the digital radiography because of its above advantages [6, 7].

A physical photograph of a direct conversion flat panel x-ray imaging detector with active matrix arrays is shown in Figure 1.2 and a simplified schematic diagram of

cross sectional structure of two pixels of a direct conversion flat panel self scanned x-ray

imaging detector is depicted in Figure 1.3.
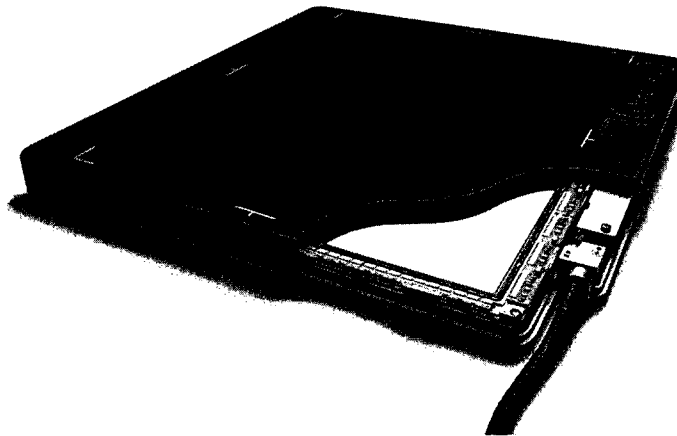
Figure 1.2 A direct-conversion flat-panel x-ray imaging detector with active matrix arrays. (Courtesy of Direct Radiography Corp.)
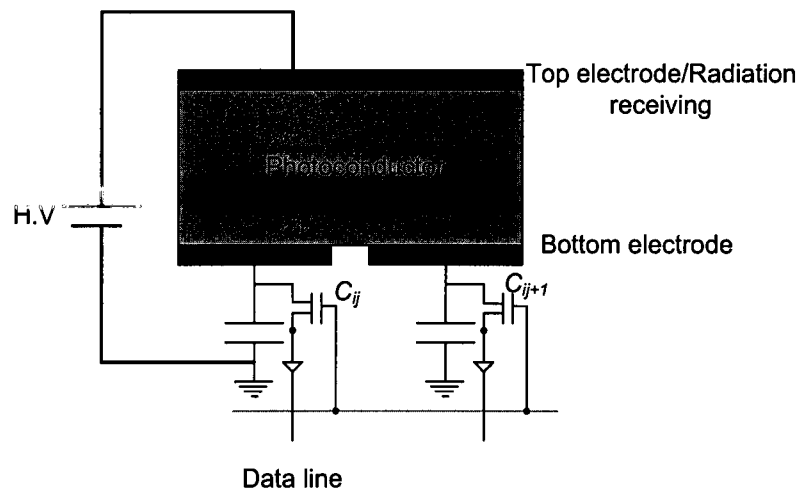
Figure 1.3 A simplified schematic diagram of the cross-sectional structure of two pixels of the photo conductive self-scanned X-ray image detector [2].

From the figure, it can be seen that a photoconductor is sandwiched between two parallel plate electrodes. The top electrode is the radiation receiving electrode and the bottom electrode is segmented into two-dimensional square pixels. Each pixel has one storage capacitor and one TFT switch. These pixels collect the generated charges and store the charge on the pixel capacitors to form a latent image. To provide an electric field within the detector, a high voltage is applied between the two electrodes. When electron-hole pairs (EHPs) are produced within the photoconductor layer due to the absorption of x-ray photons, they travel along the electric field lines across the photoconductor. The drifting of charge carriers produces a photocurrent in the external circuit. The integration of photocurrent gives the collected charge. According to the biasing of the electrodes there are two kinds of detectors. The radiation receiving electrode can be connected to either a positive bias or a negative bias with respect to the bottom electrode. The choice of bias polarity depends on the transport properties of the photoconductor.

There are three electrical connections in each thin film transistor (TFT). The 'ON' or 'OFF' state of the TFT is controlled by the gate. The drain is connected to the pixel electrode and the pixel storage capacitor (C_{ij}). The source is connected to the common data line. A large band gap (>2 eV), high atomic number semiconductor or x-ray photoconductor (e.g. stabilized amorphous selenium, a-Se) layer is coated onto the active matrix array to serve as a photoconductor layer. The capacitance of the photoconductor layer over the pixel is much smaller compared to the pixel capacitance, C_{ij}. That's why

5

most of the applied voltage drops across the photoconductor. The appropriate TFT is turned on every Δt seconds to read out the latent image charge and the charge signal is transferred to the data line. These signals are then multiplexed into a serial data line, digitized, and fed into a computer for imaging the object. A physical photograph of amorphous Selenium, a-Se based direct conversion flat panel detector is shown in Figure 1.4.
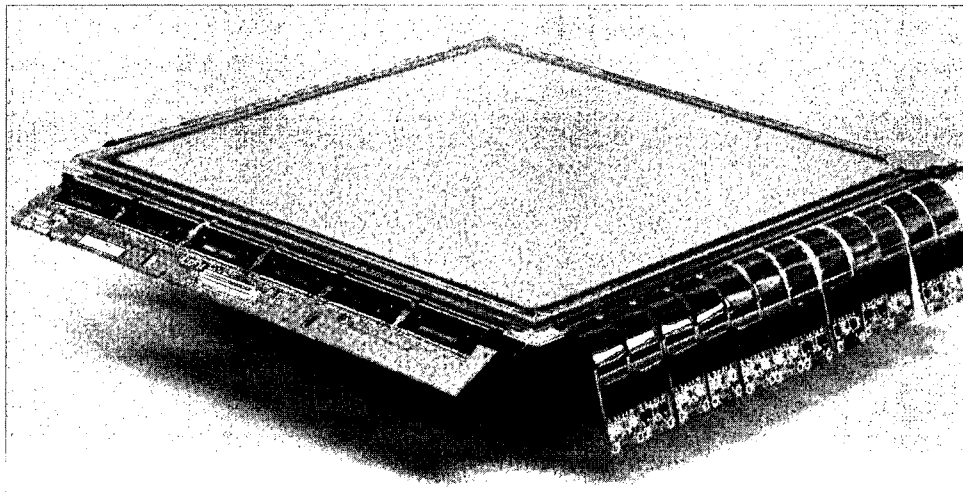
Figure 1.4 An a-Se based direct-conversion flat-panel active matrix x-ray imaging detector (Courtesy of ANRAD Corp.)

1.4 Common Requirements of X-ray Imaging Systems

There are different applications of direct conversion flat panel x-ray detector. Among them most important are chest radiology [8, 9], mammography and fluoroscopy [10, 11, 12]. The specifications of the different radiography are also different. Various medical systems mentioned previously are designed based on certain specification required for that application. Table I summarizes the common specifications for the flat panel detectors for chest radiology, mammography, and fluoroscopy.

Table I. General parameters of an x-ray imaging system for different applications. In the table, kVp is the peak value of the voltage applied to the x-ray tube for generating x-rays [4].

	Chest Radiology	**Mammography**	**Fluoroscopy**
Detector Size	35 x 43 cm^2	18 x 24 cm^2	25 x 25 cm^2
Pixel Size	200 x 200 μm^2	50 x 50 μm^2	250 x 250 μm^2
Number of Pixels	1750 x 2150	3600 x 4800	1000 x 1000
Readout time	~1s	~1s	~1/30 s
X-ray Spectrum	120 kVp	30 kVp	70 kVp
Mean Exposure	300μR	12mR	1μR
Exposure Range	30-3000μR	0.6-240mR	0.1-10μR

1.5 Ideal X-ray Photoconductor

The core of a digital imaging system is the photoconductor used between the two electrodes. The performance of the flat panel digital imaging system largely depends on the material properties and the fabrication process of the photoconductor. So, the

selection of the photoconductor is very important. In order to understand the advantages and disadvantages of our current model it is important to identify the characteristics of an ideal photoconductor. Ideally the photoconductor should have the following properties [14]:

(a) To avoid the unnecessary patient exposure, most of the x-ray radiation should be absorbed within a practical photoconductor thickness. If the absorption depth of the x rays is δ and the device layer thickness is L then according to this property: $\delta <$ L.

(b) The photoconductor should be able to generate as many collectable free electron-hole pairs as possible per unit of incident radiation. If the amount of radiation energy required for creating a single free electron-hole pair is $W_\pm$ then $W_\pm$ must be as low as possible. Generally, $W_\pm$ increases with the band gap energy E_g of the photoconductor [15].

(c) There should be no bulk recombination of EHPs. Bulk recombination is proportional to the product of the concentrations of holes and electrons. If the instantaneous x-ray exposure is not high, bulk recombination is negligible for clinical exposure rates. In this case, Auger recombination is also negligible [16].

(d) Deep trapping of carriers should be negligible for an ideal photoconductor. For both electron and hole, the schubweg $\mu\tau'F >>L$, where μ is the drift mobility, τ' is the deep trapping time (lifetime), F is the electric field and L is the detector thickness. The schubweg is the distance a carrier can travel before it is trapped by a deep trapping centre and becomes unavailable for conduction.

8

(e) The diffusion of carriers should be negligible compared with their drift which ensures less time for lateral carrier diffusion and leads to a better spatial resolution.

(f) Since the dark current(the current flow through the detector in absence of x-ray exposure) is the source of noise, it should be as low as possible. To keep the dark current low, the semiconductor-metal contact should be non- injecting and rate of thermal generation of carriers from different defects in the band gap should be negligibly small. Small dark conductivity is found in a wide band gap semiconductor that conflicts with the condition (b) above. Depending on different clinical applications, the dark current should not exceed ~10-1000 pA/cm^2 [2].

(g) Image read out time must be greater than the longest carrier transit time. Longest carrier transit time depends on the smallest drift mobility.

(h) After being exposed under the repeated number of exposure, the properties of the photoconductor should not be changed.

(i) Image lag, ghosting and these kinds of temporal artifacts should be small enough.

(j) The photoconductor should show consistent characteristics throughout its area.

(k) The photoconductor should be of such kind so that it could be easily coated on the active matrix arrays (AMA) panel.

Considering the main requirements such as large area deposition, low dark current etc., only the high bandgap amorphous and polycrystalline materials are suitable for the detector technology.

1.6 Research Motivations

Flat panel x-ray image detector based on using a direct conversion detector with an active matrix array have been shown to provide excellent images, and have been recently commercialized by a number of companies for use in diagnostic medical digital x-ray imaging applications[5]. Stabilized amorphous selenium (a-Se) is currently the best choice of photoconductor for clinical x-ray image detectors. The other potential competitors are polycrystalline Mercuric Iodide (poly-HgI_2) and polycrystalline Lead Oxide (poly-PbO)[14]. Bulk charge carrier trapping in these amorphous and polycrystalline materials strongly influences the imaging performances such as x-ray sensitivity, resolution in terms of modulation transfer function (MTF) and detective quantum efficiency (DQE) of these detectors [37,46].

Detective quantum efficiency (DQE) measures the ability of the detector to transfer signal relative to noise from its input to its output. The relative increase in image noise due to an imaging system as a function of spatial frequency, f', is expressed quantitatively by the spatial-frequency-dependent detective quantum efficiency, DQE(f'). The DQE(f') of an imaging detector is defined as,

$$DQE(f') = \frac{SNR_{out}^2(f')}{SNR_{in}^2(f')}$$

where, SNR_{in} and SNR_{out} are the signal to noise ratio at the input and output stages of an image detector, respectively. The random nature of charge carrier trapping (in general term, "incomplete charge collection") in the photoconductor layer creates fluctuations in the collected charge and hence creates additional noise. Thus carrier trapping degrades

signal to noise performance of the image and reduces DQE. The charge carrier trapping also degrades the presampling MTF [46].

In the last two decades, Chen and Doi [24], Swank [25], Metz and Vyborny [26], Boone et al. [28] conducted their research on the effect of K-fluorescence on the phosphor material and a-Se. Hillen et al. [29] conducted research on the MTF, NPS, DQE of Cesium Iodide. Due to the several advantages of active matrix flat panel imager, several theoretical and practical studies had been done on this topic in the recent years on the different photoconductive materials including a-Se and HgI_2. Recently, Zhao et al. [30] have studied the effects of K-fluorescence on DQE(f) by developing a cascaded linear system model with a combination of series and parallel processes [27]. But Zhao et al. did not consider the effects of charge carrier trapping in their model.

Later, Kabir and Kasap [38] have examined the effects of charge carrier trapping on the zero spatial frequency, DQE(0), of an imaging detector by considering depth dependent charge collection efficiency and noise in the cascaded linear system model consisting of appropriate series processes [39,40]. Recently, Kabir [41] has studied the effects of charge carrier trapping on the DQE(f) of the PbO detectors by considering the effects of bulk charge carrier trapping on the MTF and incomplete charge collection in the cascaded linear system model. Kabir's model considers series processes only as the K-fluorescence is absent in PbO for the entire diagnostic energy range up to 88 keV. However, to date no study has been performed on the combined effects of charge carrier trapping and K-fluorescence reabsorption on the DQE(f) or DQE(0).

1.7 Research Objective

The objectives of this thesis are:

(a) Developing an appropriate model for the calculation of spatial frequency dependent detective quantum efficiency, DQE(f), incorporating the combined effects of both charge carrier trapping and the reabsorption of K-fluorescence x-rays inside the photoconductor.

(b) Propose a simplified model for calculating DQE(0) considering parallel cascaded system.

(c) Analyzing the DQE model by applying the model to the published experimental data and observing the important limiting factors and modeling parameters.

This model has been developed based on a-Se and poly- HgI_2 photoconductor flat panel x-ray imaging detectors. But the same model can be used to analyze the detector made of other photoconductive material (e.g., poly-CdZnTe, PbI_2) by changing the model parameters according to the photoconductive material.

1.8 Thesis Outline

This thesis is consists of five chapters. Following this introductory chapter, few basic theories and important terminologies are discussed in chapter two. The cascaded linear system model and the calculation of DQE(f) considering the effect of charge carrier trapping and K-fluorescence reabsorption are discussed in chapter three. In chapter four, results and discussions of the model are presented. Contributions are presented and future works are suggested in chapter five.

CHAPTER 2 BACKGROUND THEORY

Background theories and important terms used for x-ray imaging systems are reviewed in this chapter. Topics discussed in this chapter are: Attenuation, Quantum Efficiency, x-ray interaction in photoconductor, Characteristic X-Rays, Ionization Energy, Average Energy, Modulation Transfer Function, Noise Power Spectrum, Detective Quantum Efficiency and transport properties of few potential photoconductors.

2.1 Attenuation

Attenuation is the removal of x-ray photons from the x-ray beam by either absorption or scattering events in the photoconductor layer. The photon fluence across the photoconductor follows the Beer-Lambert law[18]. That is, the photon fluence at the distance x from the radiation-receiving electrode is $\Phi(x)=\Phi_0e^{-\alpha x}$ where α is the linear attenuation coefficient of the photoconductor.

2.2 Quantum Efficiency

The fraction of the x-ray photons that are attenuated in the photoconductor layer is called the quantum efficiency η of the detector and η is determined by the linear attenuation coefficient α and the photoconductor thickness L as $\eta = 1 - e^{-\alpha L}$.

2.3 X-ray Interaction Mechanism in Photoconductor

The diagnostic x rays interact with matter mainly by three different mechanisms. The types of interactions are the photoelectric effect, Rayleigh scattering, and Compton scattering. The incident x rays can be completely absorbed in the medium (photoelectric effect) or scattered (Rayleigh or Compton scattering). For diagnostic x rays, the attenuation due to the photoelectric effect is much higher than that of Rayleigh and Compton scattering. These two scattering events are often neglected.

In the photoelectric interaction, the incident x-ray interacts with an electron in the medium, and all its energy is transferred to the electron. Part of this energy is used to overcome the binding energy of the electron, and the remaining fraction becomes the kinetic energy of the photoelectron. The atom becomes ionized. If the energy of the incident x-ray is less than the binding energy of the electron, photoelectric interaction with that electron is energetically unfeasible and will not occur. K-shell (inner most shell) electrons are bound more tightly to the atom (higher binding energy) than outer-shell (L-shell, M-shell, and so on) electrons. Thus, if photoelectric interaction is energetically unfeasible with K-shell electrons, interaction may still occur with an outer-shell electron. The binding energy associated with the K-shell is called the K-edge and so on. If an electron is liberated from an inner core shell, then there exists a vacancy in its parent atom. A cascade of electron transitions can take place, which can produce one or more characteristics x rays (also called fluorescent x rays) or alternately a series of irradiative transitions involving Auger electrons will take place, resulting in the complete local deposition of energy through charged particles. The characteristics x rays are named as

K-fluorescent, L-fluorescent etc. based on the electron receiving shell. The photoelectric process is illustrated in Figure 2.1 [18].
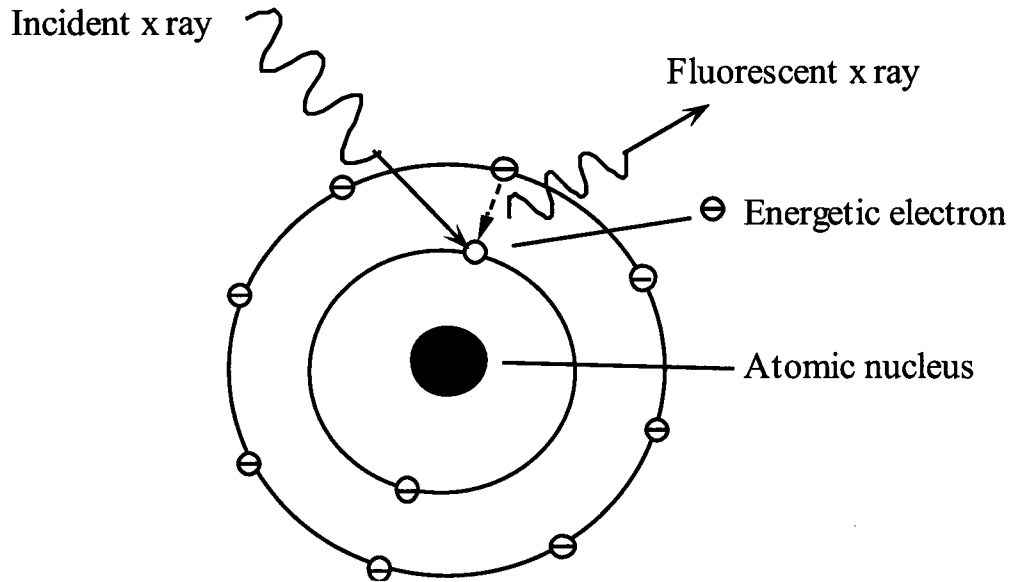
Figure 2.1 In the photoelectric effect, the energy of an incident x-ray is fully absorbed by an electron, which is ejected from the atom causing ionization. An electron from the outer shell fills the vacancy in the inner shell, which creates a fluorescent x-ray [18].

2.4 Characteristic X-Rays

There are several shells in an atom on which the electrons are orbiting around the nucleus, and those electrons are bounded by different energies. The inner-most shell is named as K-shell and the next one is named as L-shell, after that M-shell and so on, and so forth. The inner-most shell is occupied by two electrons that approximately contain the same amount of energy. On the next shell, that is the L-shell, a maximum of 8 electrons are orbiting with approximately the same energy as well. However, they possess less binding energy than those of which occupy K-shell.

Figure 2.2 [18] describes the production of characteristic x-ray. The incident x-ray photon is absorbed by the K-shell electron and when the K-shell electron obtains enough energy, it is liberated to the environment and leaves a vacancy on the K-shell. In this way a continuous electron transitions take place inside the atom starting from the filling up the vacancy on the K-shell by another electron from another atomic shell. After that a vacancy is created on that shell which is again filled by another electron from a more distant outer shell. This continues until an electron fills the outermost shell from the environment. As all the electrons from each shell have well defined discrete energies so when the electrons transit between the shells, energies are emitted in the form of photons and thus the characteristic x rays are created. Basically, characteristic x rays are generated through the photoelectric effect.
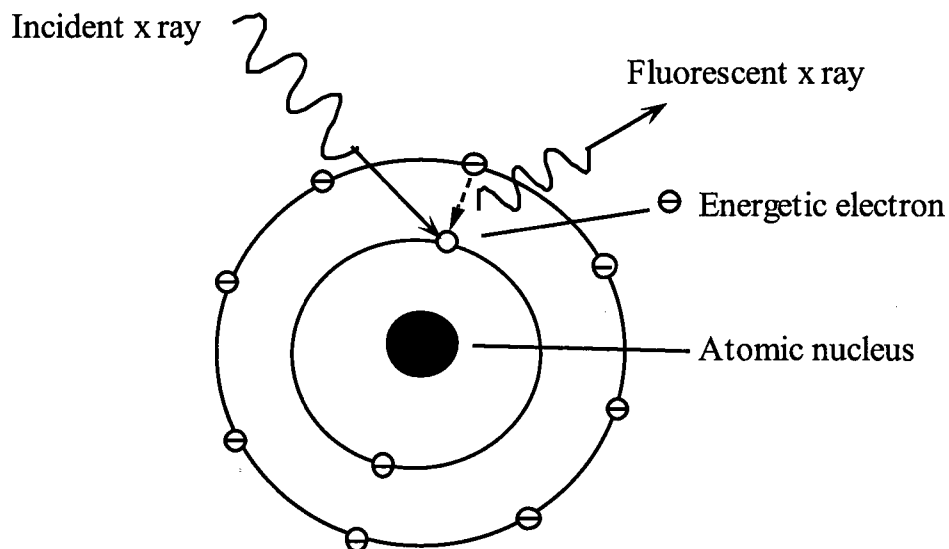
Figure 2.2 Schematic illustration of the creation of characteristic x-ray. Absorption of incident x-ray releases the electron on the innermost shell and leaves a vacancy behind. Characteristic x-ray is emitted, when an electron fills this vacancy from an outer shell [18].

As shown in the Figure 2.3 [18], the bonding energy of the K-shell electrons of Tungsten are of 70 keV, and of the L-shell are of 11 keV. When an electron from L-shell fills the vacancy on the K-shell, it requires the emission of a 59 keV x-ray photon named as K_α characteristic emission. When an electron from M-shell fills the vacancy on the K-shell it is named as K_β characteristic emission carrying the energy of 67 keV. Figure 2.3 [18] shows the L_α and L_β characteristic emissions as well, and the photon energies are 8 keV and 10.5 keV, respectively.

Tungsten Energies   Shells
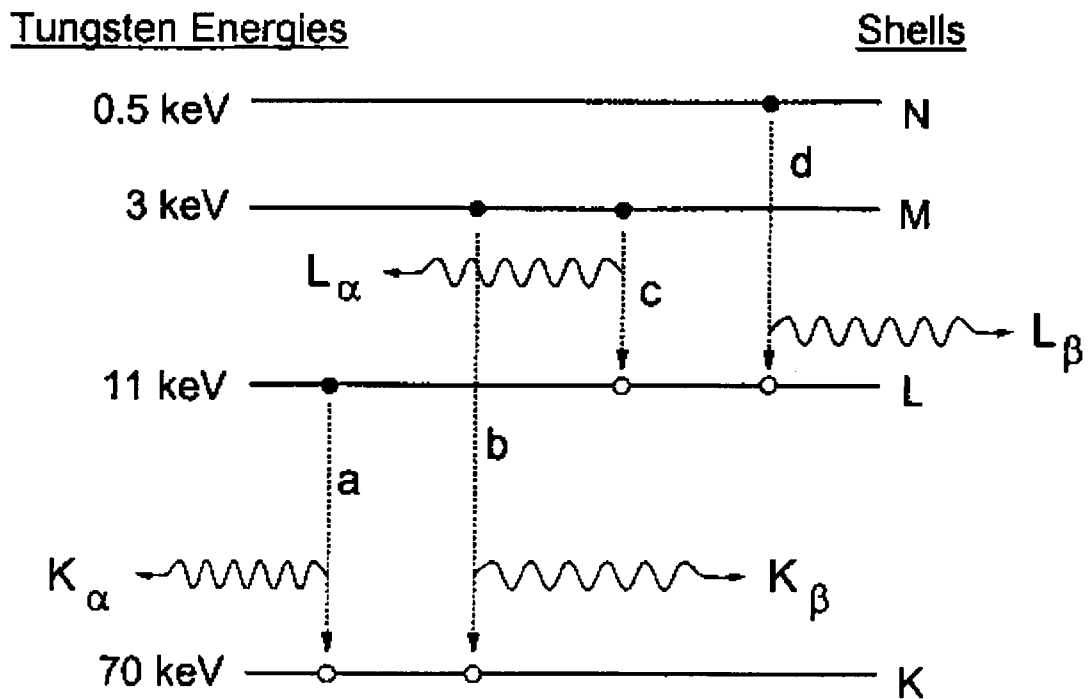
Figure 2.3 An energy diagram demonstrates the different energy levels of each shell and the emitted characteristic x-rays of Tungsten [18].

In the case where the energy of incident x-ray is less than the binding energy of an electron of the atom of the target material, the orbiting electron will not obtain enough energy to eject itself from the orbit. So, in that case there is no generation of characteristic x-ray.

2.5 Ionization Energy

The amount of radiation energy $W_\pm$ absorbed by a medium to create a single free electron-hole pair (EHP) is called the ionization energy or the EHP creation energy. This must be as low as possible because the free (or collectable) charge generated from an absorbed radiation of energy E_{ab} is simply $eE_{ab}/W_\pm$. The x-ray sensitivity of a photoconductive detector largely depends on $W_\pm$. The creation of EHPs by an incident energetic particle or an x-ray photon first involves the generation of an energetic primary electron. As this energetic photoelectron travels in the solid, it causes ionization along its track and creates many EHPs. In this way, one x-ray photon can create hundreds or thousands of EHPs. The ionization energy $W_\pm$ is the average absorbed energy required to create a single EHP. The ionization energy in a-Se depends on the electric field and it decreases as electrical field increases [19]. For amorphous-Selenium (a-Se) at the electric field of 10 V/μm, the required ionization energy is about 45 eV; whereas for polycrystalline materials like polycrystalline Mercuric Iodide (poly-HgI$_2$) and polycrystalline Cadmium Zinc Telluride (poly-CdZnTe) it is typically around 5 eV [18].

2.6 Average Energy

The x-ray beam generated by an x-ray tube is not monoenergetic but consists of a continuous spectrum of x-rays. It is often convenient to make estimates about the penetration capability or dose of an x-ray beam by assuming it is monoenergetic with some average energy. Average energy is the term used to describe an x-ray spectrum. Average energy of an x-ray spectrum is the weighted energy of the spectrum:

$$E_{ave} = \frac{\int_{E_{min}}^{E_{max}} \psi(E)dE}{\int_{E_{min}}^{E_{max}} \phi(E)dE} \tag{2.1}$$

Where, E is the energy of an x-ray photon, $\Phi(E)$ is the photon fluency (photons/mm^2) corresponding to energy E, and $\psi(E)$ is the corresponding energy fluency (joules/mm^2) where,

$$\psi(E) = \phi(E) \times E \tag{2.2}$$

2.7 Modulation Transfer Function

Modulation transfer function (MTF) measures the efficiency of an imaging system such as a detector to resolve (transfer) different spatial frequencies (fourier transform of space) of information in an image. In other words, MTF is the relative signal response of the system as a function of spatial frequency. Resolution or resolving power is the ability to record separate images of small objects that are placed very closely together.

19

The spatial resolution of an imaging device or a system can be described in terms of the MTF. The MTF of an imaging system can be described as a cascade of several stages where the overall MTF is simply the product of the MTF of all the individual stages. The MTF(f) is a much more convenient descriptor of spatial response. The dominant mechanisms responsible for the loss of resolution are: charge carrier trapping, range of primary photoelectrons, and reabsorption of K-fluorescent x-ray photons [20].

2.7.1 MTF Due to Aperture

Modulation transfer function associated with the aperture function of the pixel electrodes $T_a(f)$ arises due to averaging the signal over a pixel area. If the aperture is square with dimension a, then, $T_a(f)$ is,

$$T_a(f) = \left| \sin c(af) \right| = \left| \frac{\sin(\pi af)}{\pi af} \right| \qquad (2.3)$$

The aperture MTF describes how spatial frequencies are passed through the detector elements.

2.7.2 MTF Due to Primary Photoelectric Effect

A single diagnostic x-ray can create thousands of electron and hole pairs (EHPs). These EHPs are generated within a sphere. The size of this EHP cloud determines the spatial resolution associated with this process and is a function of the range of the

primary photoelectron. According to Que and Rowlands [20] the MTF for the finite range of primary photoelectron can be written as,

$$T_{pe}(f) = \exp\left(-\pi^2 \sigma^2 f^2\right) \qquad (2.4)$$

where, σ is a parameter proportional to the maximum range of the primary photoelectron, R_{max}. The equation (2.4) is derived based on the assumption that the maximum EHP intensity is located at the center of spherical EHP cloud and the EHP intensity versus distance from the center has the Gaussian form $exp(-x^2/\sigma^2)$. An empirical expression for R_{max} over the energy range 10-1000 keV has been given by Kanaya and Okayama [21] and that is,

$$R_{max} = 2.761 \times 10^{-5} \times \frac{M_{at} E_0^{5/3}}{\rho Z^{8/9}} \qquad (2.5)$$

where, ρ is the density (g cm^{-3}), M_{at} is the atomic mass (g mol^{-1}), Z is the atomic number, E_0 is the energy (keV) of the primary photoelectron and R_{max} is in mm. The R_{max} can be considered as the average path length and it should be smaller than the linear distance traveled by the primary electron (penetration depth). Considering this phenomenon, Que and Rowlands [20] estimated a relation between σ and R_{max} as $\sigma \approx R_{max}/2.5$.

2.7.3 MTF Due to Trapping

If a carrier is trapped in the photoconductor, it reduces signal for the corresponding pixel and induces signals on the neighboring pixels. Thus the signal is

spread out and reduces the image resolution. The equation for MTF due to the bulk carrier trapping, $T_{tr}(f)$, for a monoenergetic x-ray beam under negative bias has been given by Kabir and Kasap [46],

$$T_{tr}(E, f) = \frac{G(f)}{G(0)} \tag{2.6}$$

where,

$$G(f) = \frac{(\tau_b + \tau_t)(\omega \cos ech\omega - \exp(-1/\Delta)\omega \coth \omega - \Delta^{-1}\exp(-1/\Delta))}{\eta \Delta^2 (1 - \tau_b/\Delta)(1 + \tau_t/\Delta)(\Delta^{-2} - \omega^2)}$$

$$- \frac{(\omega \cos ech\omega - \exp(-1/\tau_b)\omega \coth \omega - \tau_b^{-1}\exp(-1/\tau_b))}{\eta \Delta (1 - \tau_b/\Delta)(\tau_b^{-2} - \omega^2)}$$

$$+ \frac{(\exp(-1/\Delta - 1/\tau_t)\omega \cos ech\omega - \exp(-1/\Delta)\omega \coth \omega + \tau_t^{-1}\exp(-1/\Delta))}{\eta \Delta (1 + \tau_t/\Delta)(\tau_t^{-2} - \omega^2)}$$

$$+ \frac{\tau_b(\exp(-1/\Delta) - \exp(-1/\tau_b))}{\eta \Delta (1 - \tau_b/\Delta)}$$

where, f is the normalized spatial frequency, $f = f'L$ and f' is the actual spatial frequency, $\omega = 2\pi f$, τ_t is the normalized lifetime of the carrier moving towards the top electrode [22],

$$\tau_t = \frac{\mu \tau'_t F}{L} \tag{2.7}$$

and τ_b is the normalized lifetime of the carrier moving towards the bottom electrode [22],

$$\tau_b = \frac{\mu \tau'_b F}{L} \tag{2.8}$$

η is the quantum efficiency of the detector and as $\eta = 1 - e^{-\alpha L}$ and $\Delta = 1/(\alpha L)$, α is the linear attenuation coefficient, L is the photoconductor thickness.

When, $f = 0$, the expression for $G(0)$ is given by [23],

$$G(0) = \frac{(\tau_b + \tau_t)(1 - \exp(-1/\Delta) - \Delta^{-1}\exp(-1/\Delta))}{\eta(1 - \tau_b/\Delta)(1 + \tau_t/\Delta)}$$

$$- \frac{\tau_b(\tau_b - \exp(-1/\tau_b) - \tau_b\exp(-1/\tau_b))}{\eta\Delta(1 - \tau_b/\Delta)}$$

$$+ \frac{\tau_t(\tau_t\exp(-1/\Delta - 1/\tau_t) + \exp(-1/\Delta) - \tau_t\exp(-1/\Delta))}{\eta\Delta(1 + \tau_t/\Delta)}$$

$$+ \frac{\tau_b(\exp(-1/\Delta) - \exp(-1/\tau_b))}{\eta\Delta(1 - \tau_b/\Delta)}$$

2.8 Noise Power Spectrum

The Noise Power Spectrum, NPS(f), describes the spectral decomposition of the noise variance, i.e., the noise variance between spatial frequencies f and $(f + df)$. X rays transmitted through a patient and incident on an imaging detector form an x-ray quantum image. The quantum image must be interpreted as distributions in the mathematical sense, having dimension area^{-1} for a two dimension image. If the two-dimensional image quanta are uncorrelated, the NPS is flat and simply equal to the expected number of quanta per unit area. For example, a uniform distribution of x rays coming from a medical x-ray tube are uncorrelated and the $NPS = \Phi_0$, where Φ_0 is the mean incident x-ray fluence (photons per unit area) on a detector. But the distribution of secondary quanta (x rays to charge carriers or light) always have an uncorrelated component, they may also

have a correlated component. Therefore, the NPS of a distribution of secondary quanta may have a frequency-dependent component extending to essentially infinite frequencies.

2.9 Detective Quantum Efficiency

Detective quantum efficiency (DQE) measures the ability of the detector to transfer signal relative to noise from its input to its output. The random nature of image quanta gives rise to random fluctuations in image signals contributing to image formation and hence creates random noises. The scattering of image quanta gives rise to image blurring which is quantified by modulation transfer function MTF(f'). Images are partially degraded by various sources of statistical fluctuations which arise along the imaging chain. The relative increase in image noise due to an imaging system as a function of spatial frequency, f', is expressed quantitatively by the spatial-frequency-dependent detective quantum efficiency, DQE(f'). The DQE(f') represents signal to noise transfer efficiency for different frequencies of information in an image. The DQE(f') of an imaging detector is defined as,

$$DQE(f') = \frac{SNR_{out}^2(f')}{SNR_{in}^2(f')} \tag{2.9}$$

where, SNR_{in} and SNR_{out} are the signal to noise ratio at the input and output stages of an image detector, respectively. DQE(f') has been considered as the appropriate metric of system performance and unity for an ideal detector.

2.10 X-ray Imaging Detector Materials

The performance of direct conversion x-ray detectors mostly depends on the design and properties of the photoconductor layer used in flat-panel detectors. The properties of an ideal photoconductor for x-ray image detectors are discussed in Section 1.5 of Chapter 1. Only amorphous or polycrystalline (poly) photoconductors are currently practical for use in large area x-ray image detectors. In this chapter, some important properties of amorphous Selenium(a-Se) and polycrystalline Mercuric Iodide (Poly-HgI_2), the two potential photoconductors for x-ray image detectors are discussed and compared with the ideal case.

2.10.1 Amorphous and Polycrystalline Solids

A perfect elemental crystal consists of a regular spatial arrangement of atoms, with precisely defined distances (the inter-atomic spacing) separating adjacent atoms. Every atom has a strict number of bonds to its immediate neighbors (the coordination) with a well defined bond length and the bonds of each atom are also arranged at identical angular intervals (bond angle). This perfect ordering maintains a long range order and hence a periodic structure.

Amorphous solid exhibits no crystalline structure or long range order and it only posses a short range orders because the atoms of amorphous solid must satisfy their individual valence bonding requirements, which leads to a little deviation in the bonding angle and length. Thus, the bonding geometry around each atom is not necessarily identical to that of other atoms, which leads to the loss of long-range order. The short

range order and long range disorder in amorphous semiconductor lead to the model of the continuous random network. The specific structural feature of a random network is the coordination of an atom to its neighbor. Thus the elementary defect of an amorphous semiconductor is the coordination defect, when an atom has either over- or under-coordination from their normal structure bonding. As a consequence of the lack of long-range order, amorphous materials do not possess such crystalline imperfections as grain boundaries and dislocations, which is a distinct advantage in certain engineering applications.

Polycrystalline material is not a single crystal as a whole, but composed of many small crystals randomly oriented in different directions. The small crystals in polycrystalline solids are called grain. Theses grains have irregular shapes and orientations as shown in Figure 2.4.

Grains

Grain boundary

The atom exists in between the grain boundaries
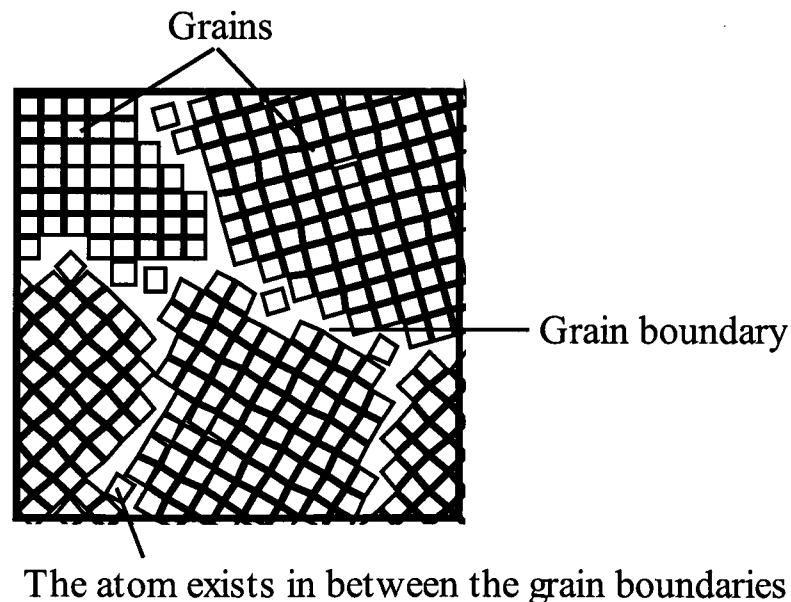
Figure 2.4 The graph demonstrates the structure of a polycrystalline solid[42]

A polycrystalline material has grain boundaries where differently oriented crystals meet. The atoms at the grain boundaries obviously cannot follow their normal bonding tendency because the crystal orientation suddenly changes across the boundary. Therefore, there are voids, and stretched and broken bonds at the grain boundary. In addition, there are misplaced atoms in grain boundary, which cannot follow the crystalline pattern on either side of the boundary. In many polycrystalline materials, impurities tend to congregate in the grain boundary region. The atomic arrangement in the grain boundary region is considered as disorder.

2.10.2 Amorphous Selenium (a-Se)

Selenium is an element of group VI of the periodic table. Chalcogen is the family name of the elements of this group. The atomic number of Selenium is 34, and in total, one Selenium atom has 28 inner core electrons and another 6 electrons on its valance band. Amorphous-Selenium (a-Se) and its alloys have been well studied due to their photo-conducting properties. The density of a-Se is 4.5 gm/cm^3, relative permittivity is 6.7 and the energy gap is 2.22 eV.

Stabilized a-Se photoconductor is one of the most preferred photoconductors used for large-area flat-panel x-ray imaging detectors for diagnostic purposes. Stabilized a-Se can be easily and quickly deposited as an uniform thin film to a large area, such as 40x40cm^2. Stabilized a-Se is commonly alloyed with 0.3% Arsenic (As) atoms and doped with ppm-level Chlorine. Another advantage of a-Se is that it can be coated by conventional vacuum deposit to form a thick film without raising the temperature of the substrate above 70°C.

Pure or crystalline Se is not suitable for x-ray photoconductors since pure a-Se is thermally unstable and crystallizes over time. The dark current resistivity of crystalline Se is much lower compared to a-Se, so it will end up with a large magnitude dark current that will degrade the x-ray image quality. In general, a-Se is alloyed with As with a range from 0.2% to 0.5% to improve the stability and prevent crystallization, but As impurity will create deep trap hole. Thus, the solution is doped in the alloy with 10-20 parts per million (ppm) of a halogen, for example Chlorine which will eliminate the side effect of As impurity by restoring the hole lifetime to its initial value. The a-Se alloyed with 0.2%-0.5% As and ppm-level Cl is called stabilized a-Se.

2.10.3 Polycrystalline Mercuric Iodide (poly-HgI$_2$)

Polycrystalline Mercuric Iodide (Poly-HgI$_2$) is under study to use in x-ray image detectors. Poly-HgI$_2$ layers have been prepared by both physical vapor deposition (PVD) and also by screen printing (SP) from slurry of HgI$_2$ crystal using a wet particle-in-binder process [17]. There appears to be no technological barrier to preparing large area layers, and direct conversion x-ray AMFPI of 20×25 cm^2 (1536×1920 pixels) and 5×5 cm^2 (512×512 pixels) size have been demonstrated using PVD and SP poly-HgI$_2$ layer, respectively [17, 43]. The prototype HgI$_2$ sensors can potentially be used for fluoroscopic or radiographic imaging. The main drawback of polycrystalline materials is the adverse effects of grain boundaries in limiting charge transport and inconsistent response of the sensor due to large grain sizes. However, there has been active research to improve the material properties of poly-HgI$_2$ based image detectors including the efforts of improving the inconsistency by reducing the grain size [43]. The band gap energy $E_g = 2.1$ eV, the

ionization energy $W_\pm \sim 5$ eV and the density of poly-HgI$_2$ is 6.3 gm/cm^3. The resistivity of this material is $\sim 4\times10^{13}$ Ω-cm [44] and the relative permittivity $\varepsilon_r = 8.3$.

HgI$_2$ tends to chemically react with various metals; hence a thin blocking layer (typically, ~ 1 μm layer of insulating polymer) is used between the HgI$_2$ layer and the pixel electrodes to prevent the reaction and also to reduce the dark current. The HgI$_2$ layer is deposited onto either conductive (ITO or gold coated) glass plates or a-Si TFT arrays. The HgI$_2$ layer thickness varies from 100-400 μm, grain size varies from 20-60 μm. A deposition of several hundred angstroms of palladium (Pd) or gold is used to form a bias (top) electrode.

HgI$_2$ image detectors with smaller grain sizes show good sensitivity and also an acceptable uniform response. The presampling MTF of these detectors is almost close to the theoretical MTF (sinc function) determined by the pixel aperture. Overall, poly-HgI$_2$ imagers show excellent sensitivity, good resolution, acceptable dark current, and homogeneity which make this material a good candidate for diagnostic x-ray image detectors.

2.10.4 Comparison between a-Se and polycrystalline materials

Amorphous selenium can be readily prepared in large areas and easily coated as thick films as mentioned earlier. It maintains consistent characteristics over large scale areas. The drawback of a-Se is that it has a very high value of electron-hole pair (EHP) creation energy of 45 eV where as the polycrystalline materials have this value of 5-6 eV range. So, a-Se needs very high voltage biasing to create the required electric field inside

the photoconductor. Very small amount of dark current[3, 13] is another positive side of using a-Se then that of polycrystalline materials [2, 15].

2.11 Summary

Necessary theoretical concepts regarding the direct conversion flat panel x-ray imaging detector have been briefly discussed in this chapter. These concepts will be very helpful to understand the model. The proposed model of frequency dependent detective quantum efficiency will be discussed in the next chapter. The model calculations, validations, fitting and discussions will be given in chapter 4.

CHAPTER 3 DETECTIVE QUANTUM EFFICIENCY (DQE)

3.1 Introduction

The detective quantum efficiency (DQE) is the appropriate metric of imaging performance for imaging detectors. The DQE measures the ability of the detector to transfer signal relative to noise from its input to its output. In most cases, the input and the output of each stage is a distribution of quanta. These quanta may be x rays, light or electrons. Images are partially degraded by various sources of statistical fluctuations which arise along the imaging chain. The relative increase in image noise due to an imaging system as a function of spatial frequency, f, is expressed quantitatively by DQE(f) which represents signal to noise transfer efficiency for different frequencies of information in an image. The DQE(f) is defined as

$$DQE(f) = \frac{SNR_{out}^2(f)}{SNR_{in}^2(f)} \tag{3.1}$$

where, SNR_{in} and SNR_{out} are the signal to noise ratio at the input and output stages of an image detector, respectively.

The DQE(f) of an imaging system depends on the MTF and NPS. When in an x-ray imaging system there is presence of K-fluorescent x rays, it will affect the overall MTF and NPS of the system. That means it will affect the DQE(f) of the system. Charge carrier trapping also creates signal blurring which is considered as a stochastic blurring process. The effect of charge carrier trapping and K-fluorescent x rays have been incorporated in the model so that more accurate theoretical analysis of the DQE(f) of an x-ray imaging detector could be possible.

3.2 Cascaded Linear System Model
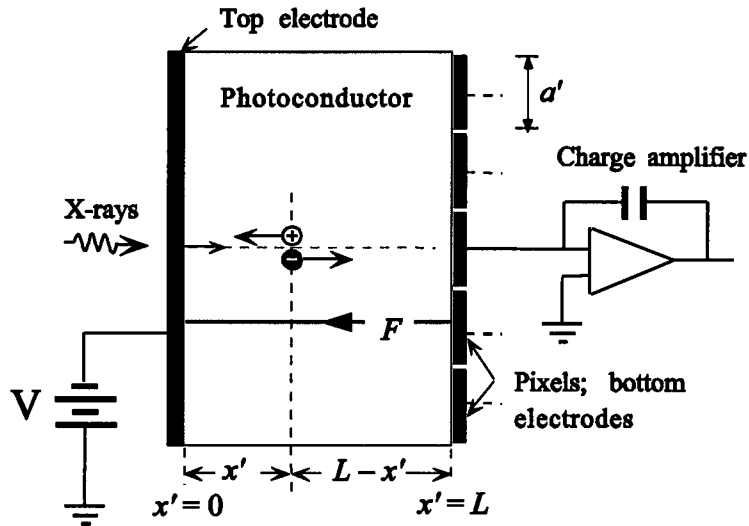
Figure 3.1 A cross section of a direct conversion pixellated x-ray image detector. An electron and a hole are generated at x' and drift under the influence of the electric field F [50].

The direct conversion x-ray imaging detector geometry consists of a photoconductor layer sandwiched between two electrodes; the electrode at one side is a continuous metal plate and the electrode on the other side of the photoconductor is segmented into an array of individual square pixels of size $a' \times a'$ as shown in Figure 3.1 [50] held at ground potential. The lateral dimension of the photoconductor slab is much greater than the photoconductor thickness L. The continuous electrode (top electrode) is biased with a voltage V to establish an electric field F in the photoconductor. As a result of image irradiation, a latent image charge accumulates on the pixel electrodes. There is a small gap between the pixel electrodes but due to electric field bending, this has negligible effect [23]. The geometric pixel aperture width in a flat panel detector is smaller than the pixel pitch (center-to-center spacing between two pixels). However, it

has been shown that the effective fill factor (the effective fraction of pixel area used for image charge collection with respect to total pixel area) of a photoconductive flat panel imager is close to unity [23, 33]. Therefore, the effective pixel aperture width is virtually identical to the pixel pitch and the detector geometry is just like a parallel plate configuration from the electrostatic point of view, except that the currents through individual pixels are integrated separately.

The diffusion of carriers is negligible compared with their drift because of high applied fields across the photoconductor. The electric field remains relatively uniform in small signals as appropriate for diagnostic applications. The general transport behavior in many direct conversion photoconductors can be described in terms of only one effective set of deep traps that controls the carrier lifetime τ' [14, 22]. Therefore, it is reasonable to assign constant drift mobility μ and a single deep trapping time (lifetime) τ' to each type of carriers (holes and electrons) [14].

The effects of charge transport properties ($\mu\tau'$) and attenuation coefficient of photoconductor materials on the detector performances depend on L and F through the following normalized parameters; the normalized attenuation depth (attenuation depth/thickness) $\Delta = 1/(\alpha L)$, the normalized electron schubweg (electron schubweg per unit thickness) $\tau_e = \mu_e\tau'_e F/L$, and the normalized hole schubweg (hole schubweg per unit thickness) $\tau_h = \mu_h\tau'_h F/L$. Here α is the linear attenuation coefficient of the photoconductor, $\mu_{e(h)}$ is the mobility, and $\tau'_{e(h)}$ is the deep trapping time (lifetime) of electrons (holes). The schubweg ($\mu\tau'F$) is the distance a carrier drifts before it is deeply trapped and unavailable for conduction. The subscripts e and h stand for electrons and

holes, respectively. Equivalently, τ_e and τ_h are the normalized carrier lifetimes (carrier lifetimes per unit transit time) for electrons and holes, respectively.

Now, If the incident x-ray fluence to a detector is $\Phi(E)$ photons per unit area per unit energy (at each photon energy E) of a polyenergetic x-ray beam, the mean input x-ray quanta Φ_0 per unit area can be calculated by integrating over the entire x-ray energy spectrum as,

$$\Phi_0 = \int_{E_{min}}^{E_{max}} \Phi(E) dE \tag{3.2}$$

where, E_{min} and E_{max} are the minimum and the maximum photon energy of the x-ray spectrum, respectively. The probability density function for an x-ray photon of energy E within an x-ray spectrum is given by,

$$p_E(E) = \frac{\Phi(E)}{\Phi_0}; \quad E_{min} \le E \le E_{max} \tag{3.3}$$

The x rays are attenuated exponentially across the photoconductor thickness. The probability density for an x-ray photon, that is attenuated within a detector, to interact at a distance x' from the top electrode is given by,

$$p_{x'}(E,x') = \left\{ \begin{array}{l} \dfrac{\alpha e^{-\alpha x'}}{\eta}, 0 \le x' \le L \\ 0, \quad \text{elsewhere} \end{array} \right\} \tag{3.4}$$

The x-ray photon energy dependent x-ray quantum efficiency $\eta(E)$ is given by,

$$\eta(E) = 1 - e^{-\alpha(E)L} \tag{3.5}$$

For simplicity, a normalized distance coordinate x is used in this thesis where $x = x'/L$; to yield the normalized pixel aperture width, $a = a'/L$ and normalized spatial frequency, $f = f'L$, in which f' is the actual spatial frequency (the convenient unit is line pairs/mm, in short, lp/mm.
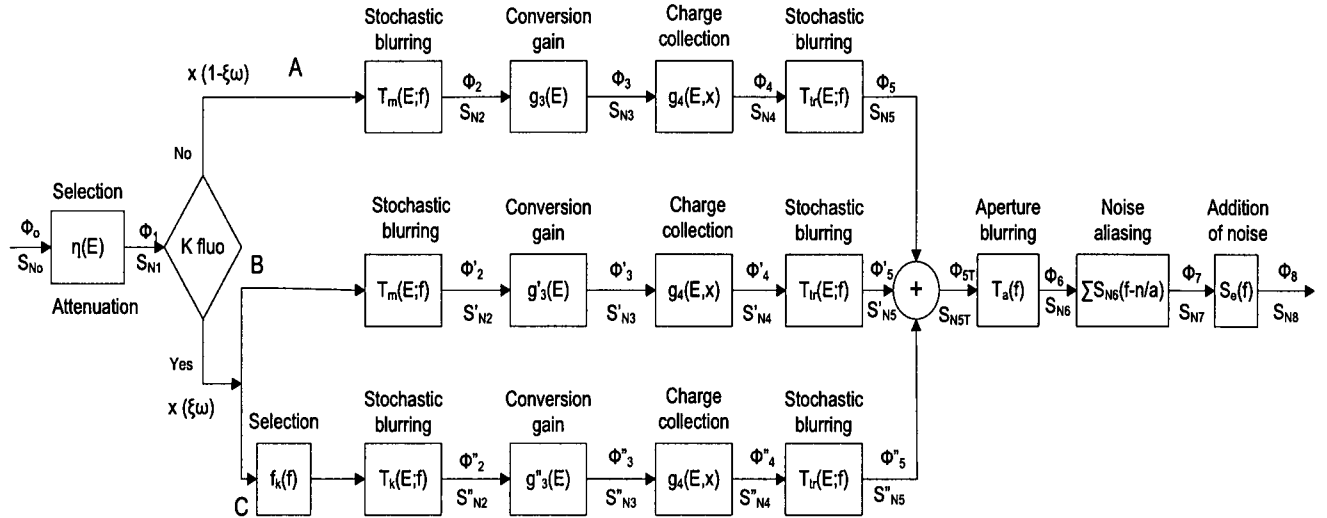
Figure 3.2 The block diagram shows the parallel and serial processes involved in the propagation of signal and NPS of an a-Se flat panel x-ray imaging detector. $x = x'/L$, normalized distance from the radiation receiving electrode; E is the incident x ray photon energy; $f = f'L$, f is the normalized spatial frequency, f' is the actual spatial frequency (the convenient unit is line-pairs/mm, in short, lp/mm)[50].

3.3 Signal and Noise Propagation

The signal and noise transfer through an x-ray image detector is a complex process. The cascaded linear-system model has been used by various investigators to characterize the performance of many imaging systems in terms of signal-transfer and noise-transfer relationships[30]. In the cascaded linear system model, an imaging system is described as cascades of simple and independent elementary stages. In the case of K-

fluorescence reabsorption and charge carrier trapping, the flow diagram of the physical processes involved in the imaging chain of a photoconductive digital x-ray detector is shown in Figure 3.2 [50]. For the creation of K-fluorescent x rays, the propagation of signal and noise after x-ray attenuation is divided into three parallel paths: (A) no K-fluorescence is generated, the attenuated incident x-ray energy is converted to charge; (B) K-fluorescent x-ray is produced, the remaining incident x-ray energy is converted to charge; and (C) when a K-fluorescent x-ray is reabsorbed remotely, its energy is converted to charge and causes image blurring. In the Figure 3.2, ξ is the probability of K-shell interaction, ω is the probability of K-fluorescence production, and f_k is the average reabsorption probability of a K-fluorescent x-ray photon within the photoconductor volume. The flow chart in Figure 3.2 consists of a combination of three parallel stages and a total of eight serial stages. The serial stages are: (1) x-ray attenuation, (2) scattering of x-ray photons before electron-hole pair (EHP) creation (this stage includes the range of primary photoelectrons in branches A & B, and reabsorption of K-fluorescent x rays in branch C), (3) the generation of charge carriers (conversion gain), (4) charge collection, (5) blurring due to charge carrier trapping, (6) aperture blurring, (7) noise aliasing, and (8) the addition of electronic noise. Each of these stages can be categorized as one of the following five processes: (i) gain, (ii) stochastic blurring, (iii) deterministic blurring, (iv) aliasing, and (v) addition.

For the gain stage i, the output mean signal quanta per unit area and noise power spectrum (NPS) arising from incident x-ray photon interactions at each depth x from the radiation-receiving electrode are, respectively [38, 39, 47],

$$\Phi_i(E,x) = g_i(E,x)\Phi_{i-1}(E,x) \tag{3.6}$$

$$S_{Ni}(E,x;f) = g_i^2(E,x)S_{N(i-1)}(E,x;f) + \sigma_{g_i}^2(E,x)\Phi_{i-1}(E,x) \tag{3.7}$$

where, $\Phi_{i-1}(E,x)$ and $S_{N(i-1)}(E,x)$ are the mean number of quanta and the NPS incident on stage i, respectively, and $g_i(E,x)$ and $\sigma_{g_i}^2(E,x)$ are the mean gain and variance of the gain of the ith stage. The selection, conversion gain and charge collection stages in Figure 3.2 are considered as the gain stage.

For the stochastic blurring stage i, the output mean signal quanta and NPS are, respectively [39, 47],

$$\Phi_i(E,x;f) = \Phi_{i-1}(E,x;f)T_i(E,x;f) \tag{3.8}$$

$$S_{Ni}(E,x;f) = T_i^2(E,x;f)S_{N(i-1)}(E,x;f) + \left[1 - T_i^2(E,x;f)\right]\Phi_{i-1}(E,x) \tag{3.9}$$

where, $T_i(E,x;f)$ is the MTF of the ith stage. The T_m, T_{tr} and T_k stages in Figure 3.2 are the stochastic blurring stage..

For the deterministic blurring stage i (e.g., the integration of signal onto individual pixels in a digital detector, the aperture blurring stage in Figure 3.2) the output mean signal quanta and NPS are, respectively [39, 47],

$$\Phi_i(E,x;f) = \Phi_{i-1}(E,x;f)T_i(E,x;f) \tag{3.10}$$

$$S_{Ni}(E,x;f) = T_i^2(E,x;f)S_{N(i-1)}(E,x;f) \tag{3.11}$$

3.4 Description of the Different Stages of the Model

Following the flow chart in Figure 3.2, the mean gain, MTF, and the variance of gain of each stage are determined as follows.

1. X-ray attenuation

An x-ray quantum incident on this selection stage either interacts with the detector, probability g_l, or does not, probability $(1- g_l)$, where g_l is the quantum efficiency η of the detector. Therefore, this is a binary selection process [39]. According to the binomial theorem, the variance of η, $\sigma_{g1}^2(E) = \eta(1-\eta)$.

Some portion of the incident x rays can be scattered and/or reflected back at metal -air and metal-semiconductor surface [18, 33]. A little fraction of the incident x-rays may be attenuated by the top metal. The dominant backscattering can occur due to the sensor structure and assembly. If the resultant fractional loss is R, then the effective quantum efficiency can be expressed as [33],

$$\eta_{eff}(E) = [1-R]\eta(E) \tag{3.12}$$

In most x-ray detector, this back scattering is controlled to a negligible level by optimizing the detector assembly and thus $R \approx 0$.

For path C, there is an additional gain(selection) stage. This gain stage will be determined by calculating the fraction of K-fluorescence reabsorbed, f_k, using the method of Dance and Day[31].

2. Stochastic scattering by the photoconductor

The scattering mechanisms in this stage include the range of primary photoelectrons, reabsorption of K-fluorescence, and reabsorption of Compton scattered photons. All these scattering take place before the creation of EHPs. The Compton scattering effect for diagnostic x rays (12 keV to 120 keV) is negligible[18]. The

dominant sources of stochastic blurring in this stage are the range of the high energy primary photoelectron in branches A and B, and the reabsorption of fluorescent x-ray photons in branch C.

A single diagnostic x-ray can create thousands of EHPs. These EHPs are generated within a sphere. The size of this EHP cloud determines the spatial resolution associated with this process and is a function of the range of the primary photoelectron. Kabir[41] has given an analytical expression to estimate the MTF, $T_m(E;f)$, due to the range of primary photoelectron.

The K-fluorescent x-ray photons can be absorbed at a point different from the primary x-ray interaction site and deteriorates the image resolution. Que and Rowlands[20] have described a method to calculate the MTF, $T_k(f)$, due to the reabsorption of K-fluorescent x rays.

3. Conversion gain

The mean conversion gain $g_3(E)$ represents the mean number of free EHPs generated after the absorption of an x-ray photon energy. The energies of the K_α and K_β fluorescent x-rays are usually very close. For simplicity, the K_α and K_β x-rays are combined as the weighted average K-line considering the relative production frequencies $I_{K\alpha}$ and $I_{K\beta}$ [38].The deposited energy considering average K-fluorescent photons is practically the same as that calculated when K_α and K_β are considered separately. The conversion gains of the three parallel paths A, B, and C are respectively [30],

$$g_3(E) = \frac{E}{W}, \quad g'_3(E) = \frac{(E - E_k)}{W}, \quad g''_3(E) = \frac{E_k}{W} \qquad (3.13)$$

where, E_k is the average energy of K-fluorescent photons and W is the EHP creation energy of the photoconductor. The fluctuations in conversion gain are due to the statistical fluctuations of the number of carriers released per x-ray photon. We assume that the mean number of free EHPs released per x-ray photon obeys a Poisson process, i.e., $\sigma_{g_3}^2(E) \approx g_3(E)$ [30] in all the branches.

4. Charge collection

Suppose that an EHP is generated at x $(x = x'/L)$ from the top electrode as shown in Figure 3.1. The average charge collection efficiency, $g_4(x)$, at the electrodes from EHP generation at coordinate x under negative bias is given by [38],

$$g_4(x) = \tau_h \left(1 - e^{-\frac{x}{\tau_h}} \right) + \tau_e \left(1 - e^{-\frac{1-x}{\tau_e}} \right) \qquad (3.14)$$

The variance of charge collection due to random trapping for an EHP generation at x is given by [40],

$$\sigma_{g_4}^2(x) = \tau_h^2 + \tau_e^2 - \tau_h^2\, e^{-\frac{2x}{\tau_h}} - \tau_e^2\, e^{-\frac{2(1-x)}{\tau_e}} - 2\tau_h x\, e^{-\frac{x}{\tau_h}} - 2\tau_e(1-x)\, e^{-\frac{(1-x)}{\tau_e}} \qquad (3.15)$$

5. Blurring by charge collection

The charge carrier trapping creates signal blurring. Since the charge carrier tapping is a random process, the signal blurring due to the carrier trapping is considered as a stochastic blurring process. The MTF due to the carrier trapping, $T_{tr}(f)$ is

determined using an analytical expression given by Kabir and Kasap [46] and discussed in section 2.7.3.

6. Deterministic Blurring by the aperture

The signal integration on each pixel causes a deterministic blurring due to averaging the signal over a pixel area. The amount of blurring, $T_a(f)$, is determined by the pixel size. If the aperture is square with dimension a, then, the MTF associated with the pixel aperture is given in equation (2.3) as,

$$T_a(f) = |\sin c(af)| = \left|\frac{\sin(\pi a f)}{\pi a f}\right|.$$

7. Noise aliasing

The digital detector is usually under-sampled since the pre-sampling signal has substantial frequency components above the Nyquist frequency, f_N. In this case, high frequency signal and/or noise above f_N are wrapped back onto the image as a lower frequency. Only NPS is affected by the signal and noise propagation through the aliasing stage [47, 48]. The overlapping frequency components of the digital NPS are simply added and thus potentially increase image noise at frequencies below f_N.

8. Addition of electronic noise

During image readout, the electronic noise power S_e associated with the TFTs and the external charge amplifiers will be added to the total noise power. The dominant sources of electronic noise are the TFT thermal noise (typical value is 600e) and the amplifier noise (typical value is 1000e-3000e). Each of the component sources of noise is

independent [45]. Therefore, the total noise power is the sum of the noise powers of all the sources. Since the electronic noise generated from each pixel is independent from each other, the total output noise power is [38], $S_{N8}=S_{N7}+S_e$.

3.5 Calculation of DQE(f) for monoenergetic x-ray beam

The input NPS in the number of x rays incident on the detector is equal to the mean photon fluence, i.e., $S_{N0}=\Phi_0$. Therefore, the square of signal to noise ratio at the input,

$$\text{SNR}_{\text{in}}^2 = \Phi_0. \tag{3.16}$$

Now, applying equations (3.6), (3.7), (3.8) and (3.9) successively we can get the output signal and NPS after each stage as stated follows:

After 1st stage:

The first stage is a stochastic gain stage. Therefore,

$$\Phi_1 = g_1 \Phi_0 = \eta \Phi_0 \tag{3.17}$$

$$
\begin{aligned}
S_{\text{N1}} &= g_1^2 S_{\text{N0}} + \sigma_{g1}^2 \Phi_0 \\
&= \eta^2 S_{\text{N0}} + \eta(1-\eta)\Phi_0 \\
&= \eta^2 \Phi_0 + \eta \Phi_0 - \eta^2 \Phi_0 \\
&= \eta \Phi_0 \\
&= \Phi_1
\end{aligned}
$$

After 2nd stage:

The second stage is a stochastic blurring stage.

For path A,

$$\Phi_2 = (1 - \xi\omega)\Phi_1 T_m = (1 - \xi\omega)\eta\Phi_0 T_m$$

$$
\begin{aligned}
S_{N2} &= (1 - \xi\omega)\{T_m^2 S_{N1} + (1 - T_m^2)\Phi_1\} \\
&= (1 - \xi\omega)(T_m^2\Phi_1 + \Phi_1 - T_m^2\Phi_1) \\
&= (1 - \xi\omega)\Phi_1 \\
&= S_{N1}(1 - \xi\omega)
\end{aligned}
$$

$$\text{So, } S_{N2} = S_{N1}(1 - \xi\omega) \tag{3.18}$$

After 3rd stage:

For path A,

$$
\begin{aligned}
\Phi_3 &= g_3\Phi_2 \\
&= g_3(1 - \xi\omega)\eta\Phi_0 T_m \\
&= (1 - \xi\omega)\eta g_3\Phi_0 T_m
\end{aligned}
$$

$$
\begin{aligned}
S_{N3} &= g_3^2 S_{N2} + \sigma_{g3}^2\Phi_2 \\
&= g_3^2 S_{N1}(1 - \xi\omega) + g_3\Phi_2 \\
&= g_3^2\Phi_1(1 - \xi\omega) + g_3(1 - \xi\omega)\eta\Phi_0 T_m \\
&= g_3\eta\Phi_0(1 - \xi\omega)(g_3 + 1)
\end{aligned}
$$

After 4th stage:

For path A,

$$\Phi_4 = \Phi_3 \int_0^L g_4 p_{x'} dx'$$

$$= (1-\xi\omega)\eta g_3 \Phi_0 T_m \int_0^L g_4 \frac{\alpha e^{-\alpha x'}}{\eta} dx'$$

$$= (1-\xi\omega)g_3 \Phi_0 T_m \alpha \int_0^L g_4 e^{-\alpha x'} dx'$$

$$= (1-\xi\omega)g_3 \Phi_0 T_m \alpha L \int_0^1 g_4 e^{-\alpha x L} dx$$

$$= (1-\xi\omega)g_3 \Phi_0 T_m \frac{1}{\Delta} \int_0^1 g_4 e^{-\frac{x}{\Delta}} dx$$

$$= (1-\xi\omega)\frac{\Phi_0}{\Delta} g_3 T_m \int_0^1 g_4 e^{-\frac{x}{\Delta}} dx$$

$$S_{N4} = \int_0^L (g_4{}^2 S_{N3} + \sigma_{g4}^2 \Phi_3) p_{x'} dx'$$

$$= \int_0^L \{g_4{}^2 g_3 \eta \Phi_0 (1-\xi\omega)(g_3 + 1) + \sigma_{g4}^2 (1-\xi\omega)\eta g_3 \Phi_0 T_m\} p_{x'} dx'$$

$$= (1-\xi\omega)g_3 \eta \Phi_0 \int_0^L \{g_4{}^2 (g_3 + 1) + \sigma_{g4}^2\} p_{x'} dx'$$

$$= (1-\xi\omega)g_3 \frac{\Phi_0}{\Delta} \int_0^1 \{g_4{}^2 (g_3 + 1) + \sigma_{g4}^2\} e^{-\frac{x}{\Delta}} dx$$

After 5th stage:

For path A,

$$\Phi_5 = T_{tr} \Phi_4$$

$$= T_{tr}(1-\xi\omega)\frac{\Phi_0}{\Delta} g_3 T_m \int_0^1 g_4 e^{-\frac{x}{\Delta}} dx$$

$$= (1-\xi\omega)\frac{\Phi_0}{\Delta} g_3 T_m T_{tr} \int_0^1 g_4 e^{-\frac{x}{\Delta}} dx$$

$$S_{N5} = T_{tr}^2 S_{N4} + (1 - T_{tr}^2)\Phi_4$$

$$= T_{tr}^2 (1 - \xi\omega)g_3 \frac{\Phi_0}{\Delta} \int_0^1 \{g_4^2(g_3 + 1) + \sigma_{g4}^2\}e^{-\frac{x}{\Delta}}dx + (1 - T_{tr}^2)(1 - \xi\omega)\frac{\Phi_0}{\Delta} g_3 T_m \int_0^1 g_4 e^{-\frac{x}{\Delta}}\,dx$$

$$= (1 - \xi\omega)g_3 \frac{\Phi_0}{\Delta}[T_{tr}^2 \int_0^1 \{g_4^2(g_3 + 1) + \sigma_{g4}^2\}e^{-\frac{x}{\Delta}}dx + (1 - T_{tr}^2)\int_0^1 g_4 e^{-\frac{x}{\Delta}}\,dx]$$

So,
$$\Phi_5 = (1 - \xi\omega)\frac{\Phi_0}{\Delta} g_3 T_m T_{tr} \int_0^1 g_4 e^{-\frac{x}{\Delta}}\,dx \tag{3.19}$$

$$S_{N5} = (1 - \xi\omega)g_3 \frac{\Phi_0}{\Delta}[T_{tr}^2 \int_0^1 \{g_4^2(g_3 + 1) + \sigma_{g4}^2\}e^{-\frac{x}{\Delta}}dx + (1 - T_{tr}^2)\int_0^1 g_4 e^{-\frac{x}{\Delta}}\,dx] \tag{3.20}$$

Similarly for path B,

$$\Phi'_5 = (\xi\omega)\frac{\Phi_0}{\Delta} g'_3 T_m T_{tr} \int_0^1 g_4 e^{-\frac{x}{\Delta}}\,dx \tag{3.21}$$

$$S'_{N5} = (\xi\omega)g'_3 \frac{\Phi_0}{\Delta}[T_{tr}^2 \int_0^1 \{g_4^2(g'_3 + 1) + \sigma_{g4}^2\}e^{-\frac{x}{\Delta}}dx + (1 - T_{tr}^2)\int_0^1 g_4 e^{-\frac{x}{\Delta}}\,dx] \tag{3.22}$$

In the same way, for path C,

$$\Phi''_5 = (\xi\omega)\frac{\Phi_0}{\Delta} g''_3 T_k T_{tr} f_k \int_0^1 g_4 e^{-\frac{x}{\Delta}}\,dx \tag{3.23}$$

$$S''_{N5} = (\xi\omega)g''_3 f_k \frac{\Phi_0}{\Delta}[T_{tr}^2 \int_0^1 \{g_4^2(g''_3 + 1) + \sigma_{g4}^2\}e^{-\frac{x}{\Delta}}dx + (1 - T_{tr}^2)\int_0^1 g_4 e^{-\frac{x}{\Delta}}\,dx] \tag{3.24}$$

For path C, there is an extra selection gain, f_k and an MTF due to reabsorption of K-fluorescence, T_k instead of MTF due to range of photoelectron, T_m.

As the path B and C are originated from the identical incident x-ray they are correlated [27]. The cross correlation of S'_{N5} and S''_{N5} is

$$S_{BC} = \eta \Phi_0(\xi\omega) \times (g'_3 \int_0^L g_4 p_{x'} dx') \times (f_k g''_3 \int_0^L g_4 p_{x'} dx') \times (T_m T_{tr}) \times (T_k T_{tr})$$

$$= \Phi_0(\xi\omega) g'_3 g''_3 f_k T_m T_{tr}^2 T_k \eta \int_0^L g_4 p_{x'} dx \int_0^L g_4 p_{x'} dx'$$

$$= \Phi_0(\xi\omega) g'_3 g''_3 f_k T_m T_{tr}^2 T_k \eta [\int_0^L g_4 \frac{\alpha e^{-\alpha'}}{\eta} dx']^2$$

$$= \Phi_0(\xi\omega) g'_3 g''_3 f_k T_m T_{tr}^2 T_k \eta [\frac{\alpha}{\eta} \int_0^L g_4 e^{-\alpha'} dx']^2$$

$$= \Phi_0(\xi\omega) g'_3 g''_3 f_k T_m T_{tr}^2 T_k \eta \frac{1}{\eta^2} [\alpha L \int_0^1 g_4 e^{-\alpha L} dx]^2$$

$$= \Phi_0(\xi\omega) g'_3 g''_3 f_k T_m T_{tr}^2 T_k \frac{1}{\eta} [\frac{1}{\Delta} \int_0^1 g_4 e^{-\frac{x}{\Delta}} dx]^2$$

$$= \Phi_0(\xi\omega) g'_3 g''_3 f_k T_m T_{tr}^2 T_k \frac{1}{\eta} \frac{1}{\Delta^2} [\int_0^1 g_4 e^{-\frac{x}{\Delta}} dx]^2$$

$$= \frac{\Phi_0}{\eta \Delta^2} (\xi\omega) g'_3 g''_3 f_k T_m T_{tr}^2 T_k [\int_0^1 g_4 e^{-\frac{x}{\Delta}} dx]^2$$

So, $$S_{BC} = \frac{\Phi_0}{\eta \Delta^2} (\xi\omega) g'_3 g''_3 f_k T_m T_{tr}^2 T_k [\int_0^1 g_4 e^{-\frac{x}{\Delta}} dx]^2 \qquad (3.25)$$

Now the total signal and NPS after the trapping MTF stage are [27],

$$\Phi_{5T} = \Phi_5 + \Phi'_5 + \Phi''_5 \qquad (3.26)$$

$$S_{N5T} = S_{N5} + S'_{N5} + S''_{N5} + 2S_{BC} \qquad (3.27)$$

After 6th , 7th and 8th stages:

$$\Phi_6 = T_a \Phi_{5T} \qquad (3.28)$$

$$S_{N6} = T_a^2 S_{N5T} \qquad (3.29)$$

As only NPS is affected by the aliasing stage, therefore,

$$\Phi_7 = \Phi_6 \tag{3.30}$$

$$S_{N7} = S_{N6} + \sum_{n=-\infty}^{\infty} S_{N6}\left(f - \frac{n}{a}\right) \tag{3.31}$$

Only electronic noise is added after the 8th stage but the signal remains the same. Therefore,

$$\Phi_8 = \Phi_7 = \Phi_6$$

$$S_{N8} = S_{N7} + S_e$$

Thus,

$$DQE(f) = \frac{SNR_{out}^2(f)}{SNR_{in}^2(f)} = \frac{\Phi_8^2(f)/S_{N8}(f)}{\Phi_0^2/S_{N0}} = \frac{\Phi_8^2(f)}{\Phi_0 S_{N8}(f)} \tag{3.32}$$

3.6 DQE(*f*) for polyenergetic x-ray beam

For the polyenergetic x-ray beam, the term Φ_0 has to be replaced by $\Phi(E)$ in equations (3.19) to (3.25) and these equations have to be integrated over the radiation spectrum of the x-ray source. So, for the polyenergetic x-ray beam, equations (3.19) to (3.25) will be as follows:

For Path A,

$$\Phi_5 = (1 - \xi\omega) \int_{E_{min}}^{E_{max}} \frac{\Phi(E)}{\Delta(E)} g_3(E) T_m(E,f) T_{tr}(E,f) \int_0^1 g_4(x) e^{-\frac{x}{\Delta}} \, dx dE \tag{3.33}$$

$$S_{N5} = (1 - \xi\omega) \int_{E_{min}}^{E_{max}} g_3(E) \frac{\Phi(E)}{\Delta(E)} [T_{tr}^2(E,f) \int_0^1 \{g_4^2(x)(g_3(E)+1) + \sigma_{g4}^2\} e^{-\frac{x}{\Delta}} dx$$

$$+ (1 - T_{tr}^2(E,f)) \int_0^1 g_4(x) e^{-\frac{x}{\Delta}} \, dx] dE \tag{3.34}$$

47

For Path B,

$$\Phi'_5 = (\xi\omega) \int_{E_{min}}^{E_{max}} \frac{\Phi(E)}{\Delta(E)} g'_3(E) T_m(E,f) T_{tr}(E,f) \int_0^1 g_4(x) e^{-\frac{x}{\Delta}} \, dx dE \qquad (3.35)$$

$$S'_{N5} = (\xi\omega) \int_{E_{min}}^{E_{max}} g'_3(E) \frac{\Phi(E)}{\Delta(E)} [T_{tr}^2(E,f) \int_0^1 \{g_4^2(x)(g'_3(E)+1) + \sigma_{g4}^2\} e^{-\frac{x}{\Delta}} dx$$

$$+ (1 - T_{tr}^2(E,f)) \int_0^1 g_4(x) e^{-\frac{x}{\Delta}} \, dx] dE \quad (3.36)$$

For Path C,

$$\Phi''_5 = (\xi\omega) \int_{E_{min}}^{E_{max}} \frac{\Phi(E)}{\Delta(E)} g''_3(E) T_k(E,f) T_{tr}(E,f) f_k \int_0^1 g_4(x) e^{-\frac{x}{\Delta}} \, dx dE \qquad (3.37)$$

$$S''_{N5} = (\xi\omega) \int_{E_{min}}^{E_{max}} g''_3(E) f_k \frac{\Phi(E)}{\Delta(E)} [T_{tr}^2(E,f) \int_0^1 \{g_4^2(x)(g''_3(E)+1) + \sigma_{g4}^2\} e^{-\frac{x}{\Delta}} dx$$

$$+ (1 - T_{tr}^2(E,f)) \int_0^1 g_4(x) e^{-\frac{x}{\Delta}} \, dx] dE \quad (3.38)$$

And the cross correlation between path B and C is

$$S_{BC} = \int_{E_{min}}^{E_{max}} \frac{\Phi(E)}{\eta(E)\Delta^2(E)} (\xi\omega) g'_3(E) g''_3(E) f_k T_m(E,f) T_{tr}^2(E,f) T_k(E,f)$$

$$\times [\int_0^1 g_4(x) e^{-\frac{x}{\Delta}} \, dx]^2 dE \qquad (3.39)$$

The equation (3.32) is still applicable for the calculation of DQE provided that we consider the terms Φ_0, Φ_{5T} and S_{N5T} as appropriate for a polyenergetic x-ray beam.

3.7 Calculation of DQE(0)

It is often convenient to calculate zero spatial frequency DQE, i.e, DQE(0). DQE(0) represents signal quality degradation due to the signal and noise transfer characteristics of the system without considering signal spreading. The flow-chart for DQE(0) model is shown in Figure 3.3.
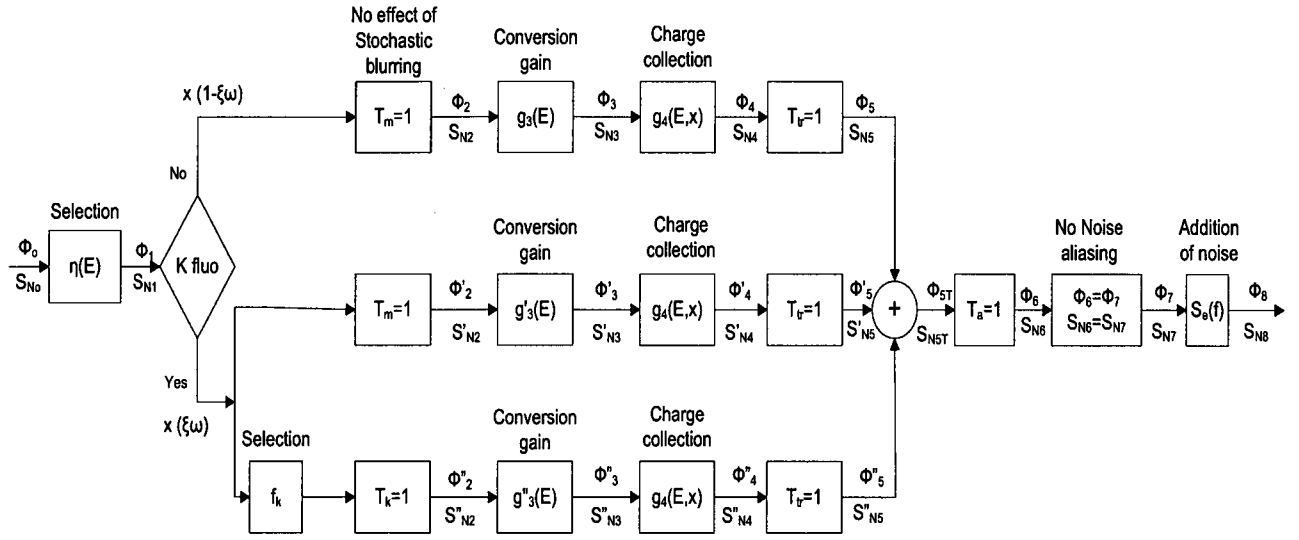
Figure 3.3 The block diagram shows the parallel and serial processes involved in the propagation of signal and NPS of an a-Se flat panel x-ray imaging detector when f=0.

To calculate DQE(0), we need to re consider all the equations from 2nd stage to the last stage by putting the value of T_m, T_k, T_a, T_{tr} as unity. So in 5th stage from equation (3.19) to (3.25), if we replace T_m, T_k, T_{tr} by unity then we get,

$$\Phi_5 = (1 - \xi\omega)\frac{\Phi_0}{\Delta} g_3 \int_0^1 g_4 e^{-\frac{x}{\Delta}} dx \qquad (3.40)$$

$$S_{N5} = (1 - \xi\omega)g_3 \frac{\Phi_0}{\Delta} \int_0^1 \{g_4^2(g_3 + 1) + \sigma_{g4}^2\}e^{-\frac{x}{\Delta}} dx \qquad (3.41)$$

$$\Phi'_5 = (\xi\omega)\frac{\Phi_0}{\Delta}g'_3\int_0^1 g_4 e^{-\frac{x}{\Delta}}\,dx \tag{3.42}$$

$$S'_{N5} = (\xi\omega)g'_3\frac{\Phi_0}{\Delta}\int_0^1\{g_4^2(g'_3+1)+\sigma_{g4}^2\}e^{-\frac{x}{\Delta}}dx \tag{3.43}$$

$$\Phi''_5 = (\xi\omega)\frac{\Phi_0}{\Delta}g''_3 f_k\int_0^1 g_4 e^{-\frac{x}{\Delta}}\,dx \tag{3.44}$$

$$S''_{N5} = (\xi\omega)g''_3 f_k\frac{\Phi_0}{\Delta}\int_0^1\{g_4^2(g''_3+1)+\sigma_{g4}^2\}e^{-\frac{x}{\Delta}}dx \tag{3.45}$$

$$S_{BC} = \frac{\Phi_0}{\eta\Delta^2}(\xi\omega)g'_3 g''_3 f_k[\int_0^1 g_4 e^{-\frac{x}{\Delta}}\,dx]^2 \tag{3.46}$$

Now the total signal after the 5th stage is,

$$
\begin{aligned}
\Phi_{5T} &= \Phi_5 + \Phi'_5 + \Phi''_5 \\
&= \frac{\Phi_0}{\Delta}\{(1-\xi\omega)g_3 + \xi\omega g'_3 + \xi\omega f_k g''_3\}\int_0^1 g_4 e^{-\frac{x}{\Delta}}\,dx \\
&= \frac{\Phi_0}{\Delta}\{g_3 - \xi\omega(g_3 - g'_3) + \xi\omega f_k g''_3\}\int_0^1 g_4 e^{-\frac{x}{\Delta}}\,dx \\
&= \frac{\Phi_0}{\Delta}\{g_3 - \xi\omega g''_3 + \xi\omega f_k g''_3\}\int_0^1 g_4 e^{-\frac{x}{\Delta}}\,dx \\
&= \frac{\Phi_0}{\Delta}\{g_3 - (1-f_k)\xi\omega g''_3\}\int_0^1 g_4 e^{-\frac{x}{\Delta}}\,dx
\end{aligned}
$$

Comparing the output signal Φ_{5T} of the parallel cascaded system with that of the series cascaded system of Ref. [38], the equivalent conversion gain considering three parallel path can be written as,

$$g_{3,eq} = g_3 - (1 - f_k)\xi\omega g''_3 \tag{3.47}$$

The total NPS after the 5th stage is,

$$S_{N5T} = S_{N5} + S'_{N5} + S''_{N5} + 2S_{BC}$$

After the 6th stage, as T_a is unity, so from equations (3.28) and (3.29) we get,

$$\Phi_6 = \Phi_{5T} \text{ and } S_{N6} = S_{N5T}.$$

After the 7th stage, when $f=0$ then there is no noise aliasing occurs. So, from equation (3.31) we get,

$$S_{N7} = S_{N6}$$

So, after 8th stage we get,

$$\Phi_8 = \Phi_7 = \Phi_6 = \Phi_{5T}$$

$$S_{N8} = S_{N7} + S_e = S_{N6} + S_e = S_{N5T} + S_e$$

So, equation (3.32) becomes,

$$DQE(0) = \frac{SNR_{out}^2(0)}{SNR_{in}^2(0)} = \frac{\Phi_8^2}{\Phi_0 S_{N8}} = \frac{\Phi_{5T}^2}{\Phi_0(S_{N5T} + S_e)} \tag{3.48}$$

51

3.8 Summary

In this chapter, the proposed cascaded linear system model, which consists of series and parallel processes, has been discussed. The signal and noise after each stage of the DQE model have been given. In the next chapter, the proposed model is applied for fluoroscopic and mammographic applications based on a-Se and HgI_2 photoconductive direct conversion x-ray imaging detectors and results are compared with the published experimental data.

CHAPTER 4 RESULTS AND DISCUSSIONS

4.1 Introduction

The model calculations and analysis of DQE(f) of a-Se and HgI$_2$ based x-ray imaging detector for the fluoroscopic and mammographic applications are presented in this chapter. In the proposed model, all the calculations are performed at 52-60 keV x-ray photon energy, which is above the K-edge of Iodine but below that of Mercury. In HgI$_2$, there is K-fluorescence emission from the Iodine atoms only. The weighted average K-fluorescent x-ray photon energies from Selenium and Iodine atoms are 11.37 and 29.28 keV, respectively.

The K-fluorescence reabsorption probability, f_k is calculated using the method of Dance and Day [31]. The attenuation coefficients are taken from the Ref. [20]. The MTF, $T_k(f)$, due to the reabsorption of K-fluorescent x rays is calculated by the method described by Que and Rowlands [20]. The MTFs $T_m(f)$ and $T_{tr}(f)$ are calculated using the analytical expressions given in the Refs. [41] and [46], respectively.

For monoenergetic x-ray beam, the expected signals Φ_{N5T}, Φ_{N6}, Φ_{N7}, Φ_{N8} and quantum noises S_{N5T}, S_{N6}, S_{N7}, S_{N8} are calculated and finally using the equation (3.32), DQE(f) for the monoenergetic x ray beam has been calculated.

4.2 Fluoroscopic Applications

The DQE(f) performance of the a-Se and poly-HgI$_2$ x-ray detectors are examined for fluoroscopic (70 kVp with 23.5 mm total Al filtration, where the average photon energy is $\approx$ 52 keV) applications. The incident x-ray exposure (X) varies from 0.1 μR to 10 μR for fluoroscopic applications. For simplicity and clarity, all the calculations in this thesis are performed using average monoenergetic x rays. Unless otherwise stated, we assume that the pixel area, A = 200 μm × 200 μm and effective fill factor is 1.0 for all types of photoconductors. The additive electronic noise ($N_e = \sqrt{S_{Ne}}$) is assumed to be 2500e per pixel. The following transport and operating parameters are used: for a-Se detectors, μ_e = 0.003 cm^2/V-s, μ_h = 0.12 cm^2/V-s, L = 1000 μm, F = 10 V/μm, W $\approx$ 43 eV [22], and for poly-HgI$_2$ detectors, L = 250 μm, F = 0.5 V/μm, W = 5 eV. The radiation-receiving electrode is biased negatively for both a-Se and poly-HgI$_2$ detectors. The K-fluorescence related constants for a-Se and HgI$_2$ are given in Table II.

Table II. K-fluorescence related constants for a-Se and HgI$_2$[49, 51]

Material	a-Se	Hg	I
K-edge energy (keV)	12.7	83.1	33.2
K-shell contribution to photo-electric (ξ)	0.864	0.795	0.838
K-fluorescence yield (ω)	0.596	0.96	0.884
Probability of K$_\alpha$ and K$_\beta$ production	0.862, 0.138	0.783, 0.217	0.814, 0.186
K$_\alpha$ and K$_\beta$ fluorescence energy (keV)	11.2, 12.5	70.8, 70.2	28.6, 32.3

4.2.1 Fluoroscopic Applications for a-Se

Figures 4.1(a) and 4.1(b) show the DQE of a-Se detectors as a function of spatial frequency for various levels of electron and hole lifetimes, respectively. The a-Se detector is exposed to 4 μR exposure at photon energy of 52 keV (monoenergetic beam) and is biased negatively. The quantum efficiency is 0.77, which is the maximum achievable DQE. The DQE monotonously decreases with increasing spatial frequency. Both electron's and hole's drift mobilities in a-Se are reasonably well defined so that $\mu\tau'$ products depend primarily on the carrier lifetimes [22].

In a-Se photoconductors, the electron lifetime (τ'_e) is in the range of 50-1500 μs whereas the hole lifetime (τ'_h) is in the range of 1-200 μs [14]. The DQE decreases with decreasing the electron lifetimes and it drops drastically if the electron lifetime is lower than 200 μs as shown in Figure 4.1(a). The DQE remains unchanged if the hole lifetime is higher than 50 μs as shown in Figure 4.1(b). It is clear from figures 4.1(a) and 4.1(b) that the DQE is much more dependent on electron lifetime than hole lifetime for the negative bias, the opposite is true for the positive bias.
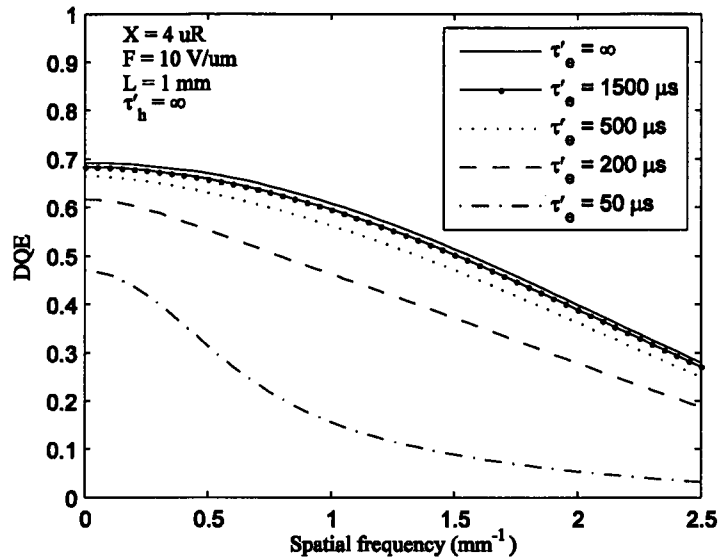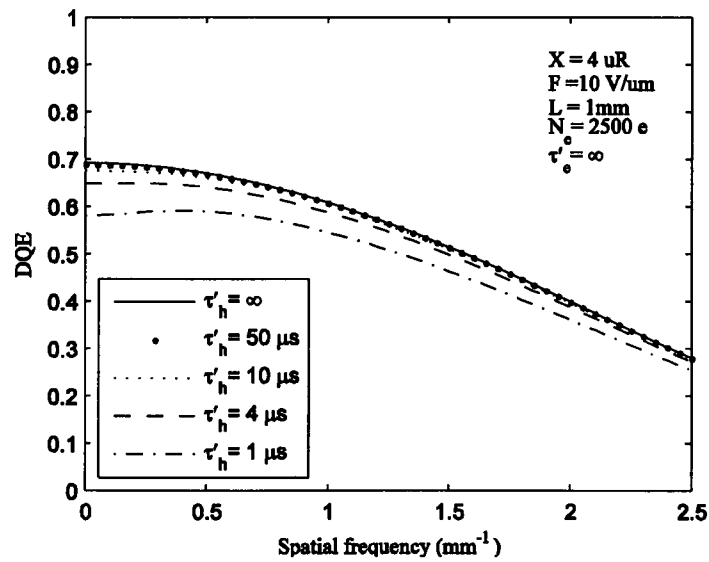
Figure 4.1 The theoretical DQE for fluoroscopy in a negatively biased a-Se detector. (a) DQE versus spatial frequency with no hole trapping (hole lifetime, $\tau'_h = \infty$) for various levels of electron lifetimes (τ'_e). (b) DQE versus spatial frequency with no electron trapping (electron lifetime, $\tau'_e = \infty$) for various levels of hole lifetimes (τ'_h).
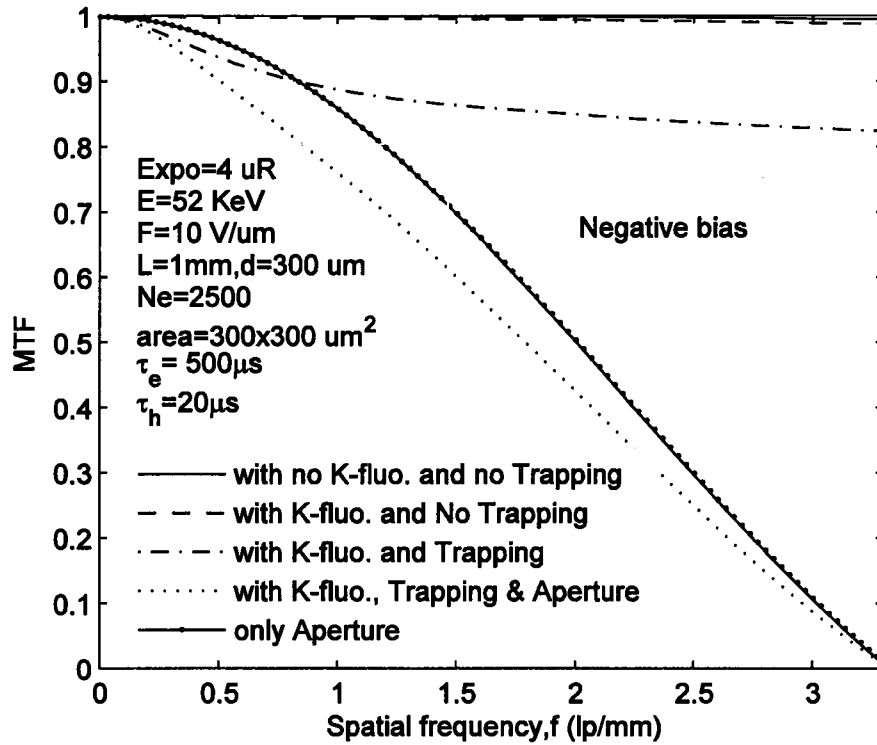
Figure 4.2 MTF versus spatial frequency considering the effects of K-fluorescence, trapping and aperture for the fluoroscopic application of a-Se x-ray imaging detector.

The MTFs due to the various scattering mechanisms are shown in Figure 4.2. It is found that the signal scattering due to K-fluorescence is very small for the photon energy of 52 keV. The incident photon energy is far from the K-edge(12.6 keV) of a-Se and thus the relative effect of K-fluorescence is very small. The difference between the dashed and the dot-dashed line represents the effect of trapping on MTF. It is clear that the bulk carrier trapping has a significant effect on the MTF.

(a)

(b)

Figure 4.3 The theoretical DQE(0) for fluoroscopy in a negatively biased a-Se detector. (a) DQE(0) versus Detector thickness with no hole trapping (hole lifetime, $\tau_h = \infty$) for various levels of electron lifetimes (τ_e). (b) DQE versus Detector thickness with no electron trapping (electron lifetime, $\tau_e = \infty$) for various levels of hole lifetimes (τ_h).
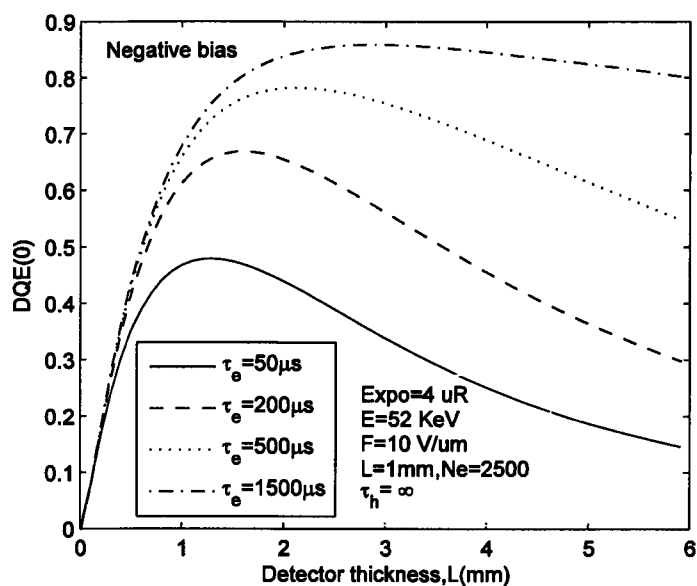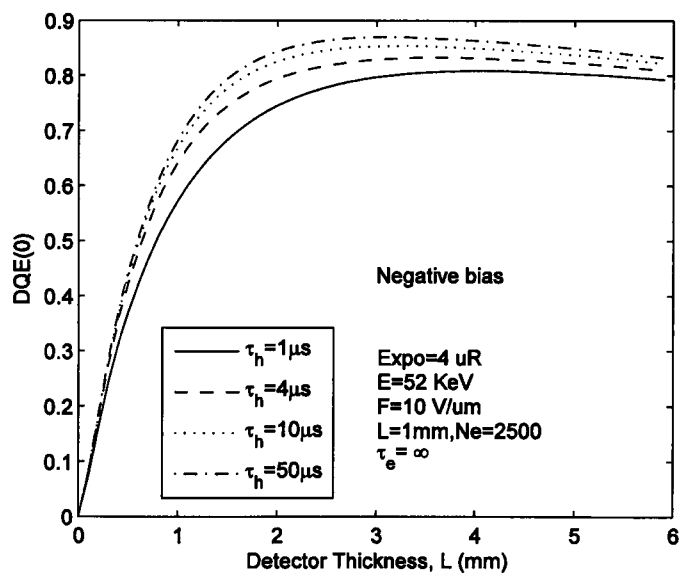
It is instructive to examine the effects of the detector thickness on the DQE. The DQE(0) vs. detector thickness as a function of carrier lifetimes is show n in Figure 4.3. There exists an optimum detector thickness that maximizes the DQE. The quantum efficiency increases and the charge collection efficiency decreases with increasing the thickness. The combined effect shows an optimum detector thickness. However, the optimum detector thickness decreases with decreasing carrier lifetimes. It is evident from Figure 4.3(a) and 4.3(b) that the DQE(0) critically depends on the electron lifetimes under negative bias. The opposite should be true under positive bias.

4.2.2 Fluoroscopic Applications for HgI_2

Figures 4.4(a) and 4.4(b) show the DQE of poly-HgI_2 detectors as a function of spatial frequency for various levels of electron and hole mobility-lifetime products, respectively. The HgI_2 detector is exposed to 4 μR exposure at photon energy of 52 keV (monoenergetic beam) and is biased negatively. The quantum efficiency is 0.76. The DQE in HgI_2 detectors also monotonously decreases with increasing spatial frequency. The lower frequency components in DQE are mainly controlled by the electron transport and DQE decreases with decreasing $\mu_e \tau'_e$. The DQE also decreases with decreasing $\mu_h \tau'_h$. However, like a-Se, the DQE is much more dependent on $\mu_e \tau'_e$ than on $\mu_h \tau'_h$ under negative bias.
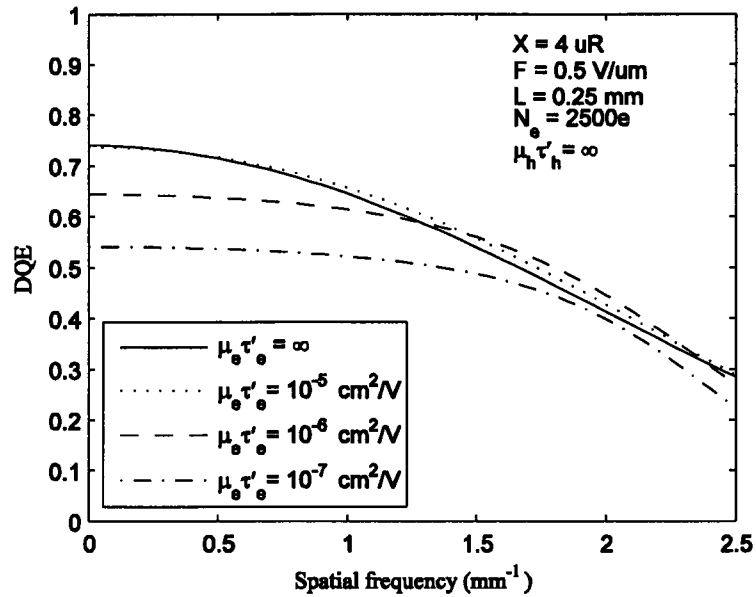
(a)
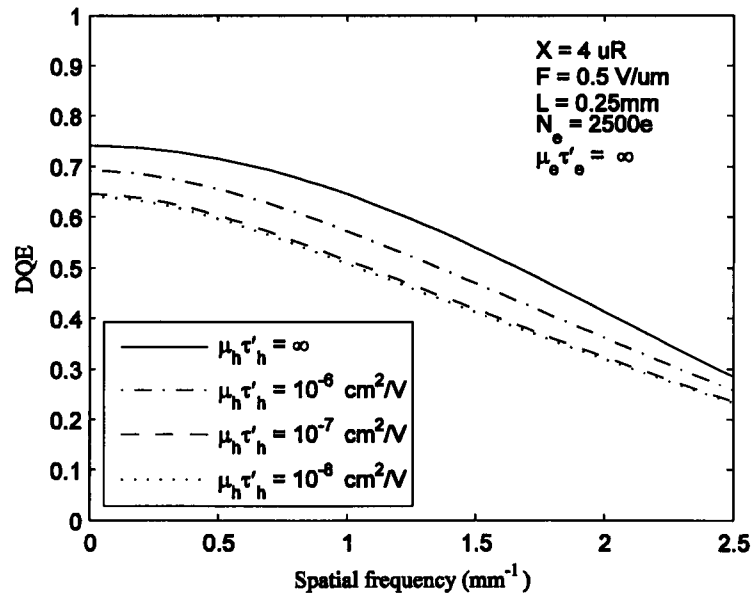
(b)

Figure 4.4 The theoretical DQE for fluoroscopy in a negatively biased poly-HgI$_2$ detector. (a) DQE versus spatial frequency with no hole trapping ($\mu_h\tau'_h = \infty$) for various levels of $\mu_e\tau'_e$. (b) DQE versus spatial frequency with no electron trapping ($\mu_e\tau'_e = \infty$) for various levels of $\mu_h\tau'_h$.
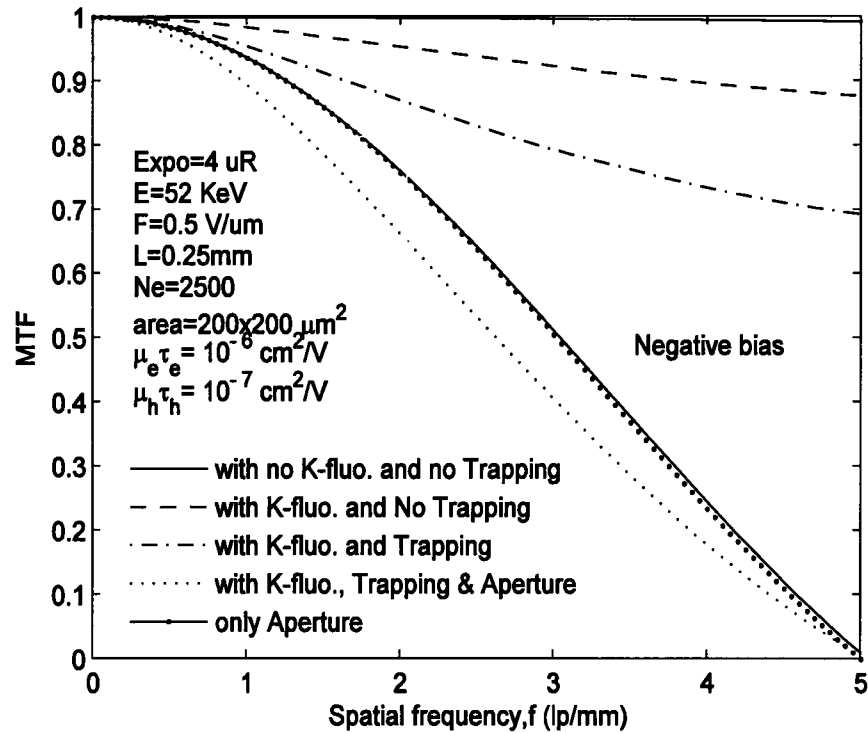
Figure 4.5 MTF versus spatial frequency considering the effects of K-fluorescence, trapping and aperture for fluoroscopic application of HgI_2 x-ray imaging detector.

The MTFs due to the various scattering mechanism in HgI_2 detectors for fluoroscopic applications are shown in Figure 4.5. The signal scattering due to the range of the primary photoelectron is negligible. The signal scattering due to the K-fluorescence reabsorption is quite significant since the K-edge of $I_2(33.2$ keV) is closer to the incident photon energy (52 keV). The charge carrier trapping also has a significant effect on the MTF.

(a)

(b)

Figure 4.6 The theoretical DQE(0) for fluoroscopy in a negatively biased poly-HgI$_2$ detector. (a) DQE(0) versus Detector thickness with no hole trapping ($\mu_h \tau_h$ = ∞) for various levels of $\mu_e \tau_e$. (b) DQE(0) versus Detector thickness with no electron trapping ($\mu_e \tau_e$ = ∞) for various levels of $\mu_h \tau_h$.
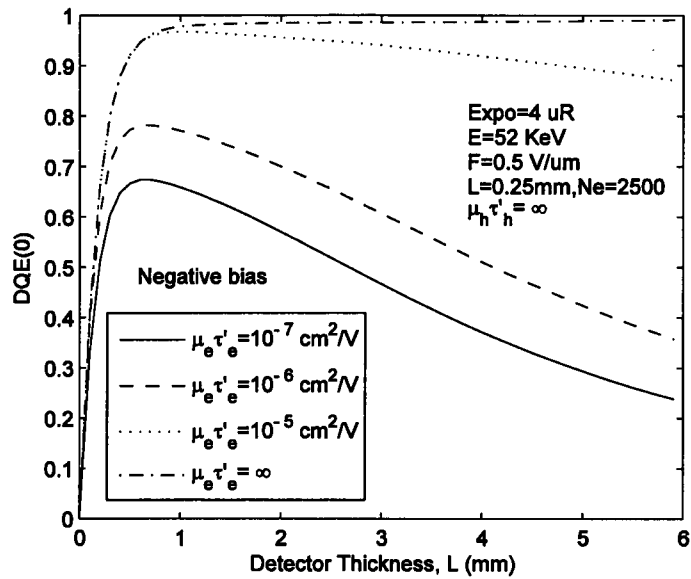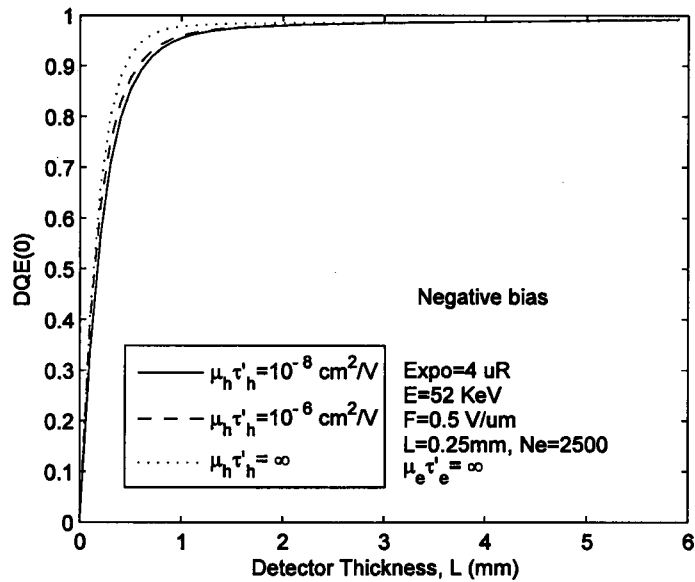
The DQE(0) versus detector thickness as a function of electron and hole ranges(mobility-lifetime product) in HgI$_2$ detector are shown in Figure 4.6. Like in the a-Se detectors, there exists an optimum detector thickness for finite electron ranges under negative bias.

4.2.3 Comparison between a-Se and HgI$_2$ based detector performance

The charge carrier transport ($\mu\tau'$ products) properties have higher influences on DQE performance in a-Se detectors than that in HgI$_2$ detectors, because of relatively low conversion gain in a-Se detectors. For example, $W \approx 43$ eV in a-Se at $F = 10$ V/μm, whereas $W = 5$ eV in poly-HgI$_2$ detectors. Both high conversion gain and high charge collection efficiency are required to improve the DQE performance of an x-ray image detector [14]. The conversion gain depends on W, which is a material property of the photoconductor. The charge collection efficiency can be improved by increasing F and improving the $\mu\tau'$ products of the carriers. However, increasing F also increases the dark current dramatically in HgI$_2$ detectors. Thus there is a practical limitation on F. An F as high as 20 V/μm is achievable in a-Se detectors while keeping the dark current within an acceptable level for x-ray imaging [32]. The charge collection efficiency of a-Se detectors is relatively high because of the high F needed to obtain a reasonable W.

4.3 Model Validation for Fluoroscopy

The DQE(f) model is fitted to the published experimental data on a-Se and HgI$_2$ detectors. Figure 4.7 shows the DQE(f) as a function of spatial frequency for a negatively biased a-Se detector of 1 mm thickness at 75 kVp x-ray exposure with 39.7

mm Al filtration. The exposure is 4.4 μR and the average x-ray photon energy is 59 keV. The open circles represent the experimental data, the dashed line represents theoretical DQE without considering trapping (no trapping means $g_4 = 1$ and $T_{tr}(f) = 1$) and K-fluorescence (no K-fluorescence means $\omega = 0$), the dotted line represents theoretical DQE without considering K-fluorescence, and the solid line represents the theoretical fit of the present model to the experimental data.

Figure 4.7 DQE versus spatial frequency for a negatively biased a-Se detector of 1 mm thickness at 75 kVp x-ray exposure with 39.7 mm Al filtration. The experimental data have been extracted from Figure 16 of Ref. [33].

In Figure 4.7, the experimental data have been extracted from Figure 16 of Ref. [33]. The exposure is 4.4 μR and the average x-ray photon energy is ≈ 59 keV. Thickness L=1mm, pixel area, A = 300 μm × 300 μm and the electronic noise is assumed to be

7200e per pixel. The theoretical model fits well with the experimental data with $\tau'_e =$ 1200 μs and $\tau'_h = 50$ μs. The K-fluorescence has negligible effect on DQE because the average photon energy (59 keV) is much higher than the K-edge (12.5 keV in a-Se).
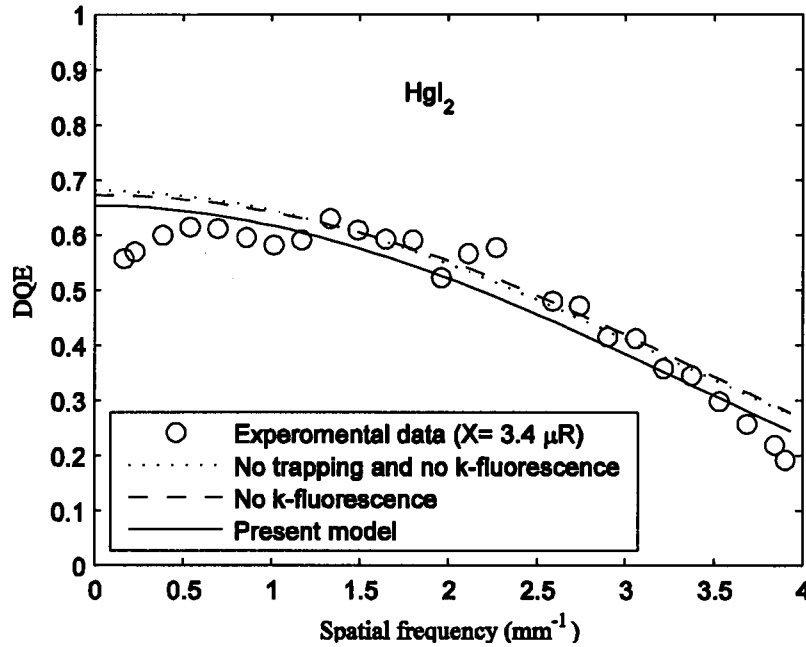
Figure 4.8 DQE versus spatial frequency for a negatively biased HgI_2 detector of 210 μm thickness at 72 kVp x-ray exposure with 23.2 mm Al filtration. The experimental data have been extracted from Figure 13 of Ref. [34].

Figure 4.8 shows the DQE as a function of spatial frequency for a negatively biased HgI_2 detector of 210 μm thickness at 72 kVp x-ray exposure with 23.2 mm Al filtration. The exposure is 3.4 μR and the average x-ray photon energy is ≈ 53 keV. The open circles represent the experimental data, the dotted line represents theoretical DQE without considering trapping and K-fluorescence, the dashed line represents theoretical DQE without considering K-fluorescence, and the solid line represents the theoretical fit of the DQE model to the experimental data. The experimental data have been extracted
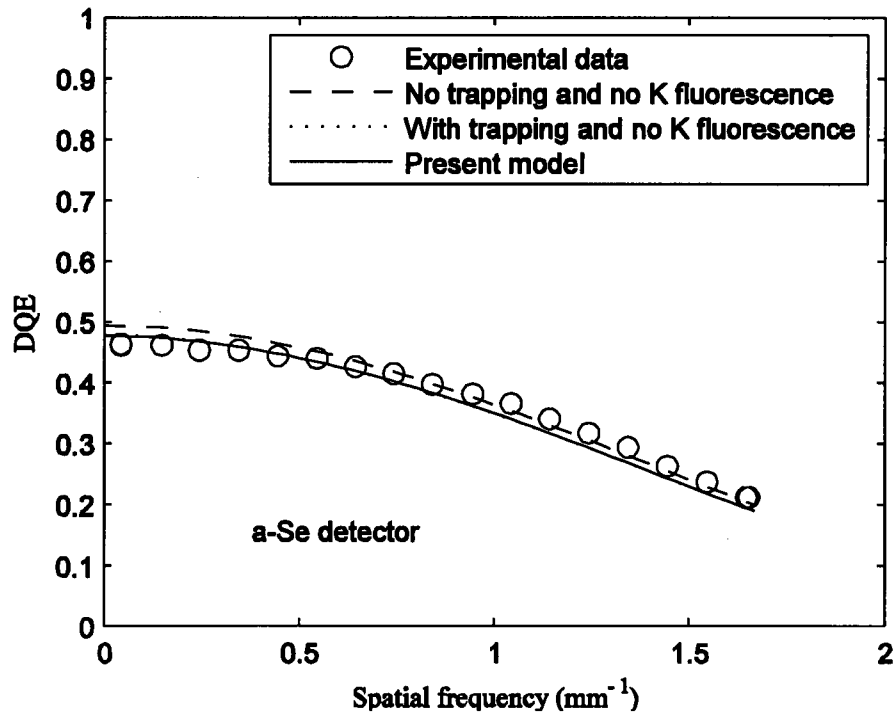
from Figure 13 of Ref. [34]. The pixel area, A = 127 μm × 127 μm and the electronic noise is assumed to be 2000e per pixel. The theoretical model fits well with the experimental data with $\mu_e\tau'_e = 10^{-5}$ cm^2/V-s and $\mu_h\tau'_h = 3 \times 10^{-6}$ cm^2/V-s. The charge carrier trapping slightly decreases the very low frequency components but improves higher frequency components of DQE. The carrier trapping reduces both MTF and NPS(f) in the frequencies above the Nyquist frequency, and thus reduces aliased noises below f_N and improves the DQE(f) performance [35]. The K-fluorescence reabsorption has a significant effect on DQE because the average photon energy (53 keV) is close to the K-edge (33.2 keV) of Iodine in HgI$_2$.

4.4 Mammographic Applications

Using the proposed model, the DQE(f) performance of an a-Se direct conversion x ray detector is examined for mammographic applications. The pixel area is equal to 200×200 μm^2, average energy 20 keV and the additive electronic noise is 2500 electrons. Incident x-ray exposure 12 mR and electric field 10 V/μm are used in the calculation. The thickness of the detector is L=200 μm.

Figures 4.9(a) and 4.9(b) show the DQE of positively biased a-Se detectors as a function of spatial frequency for various levels of electron and hole lifetimes, respectively, for mammographic applications. The a-Se detector is exposed to 12 mR exposure at photon energy of 20 keV (monoenergetic beam). The DQE monotonously decreases with increasing spatial frequency. Both electron's and hole's drift mobilities in a-Se are reasonably well defined so that μτ products depend primarily on the carrier lifetimes [22].
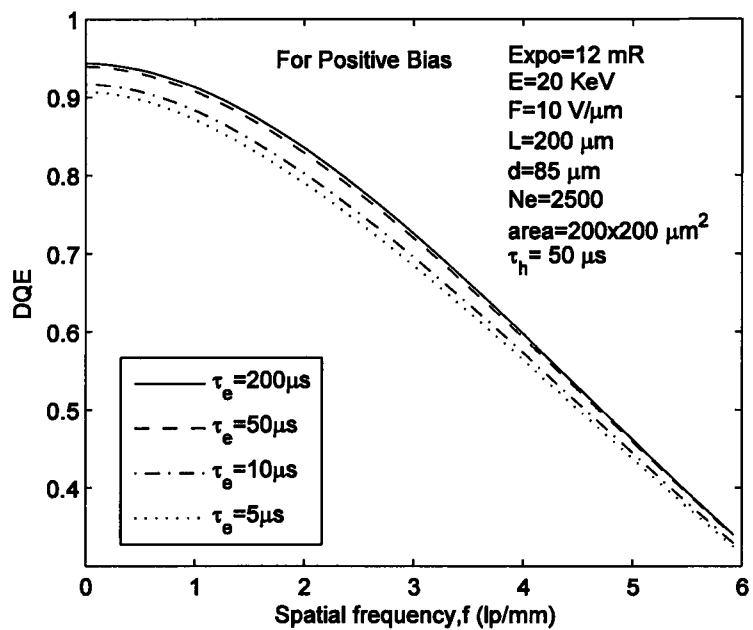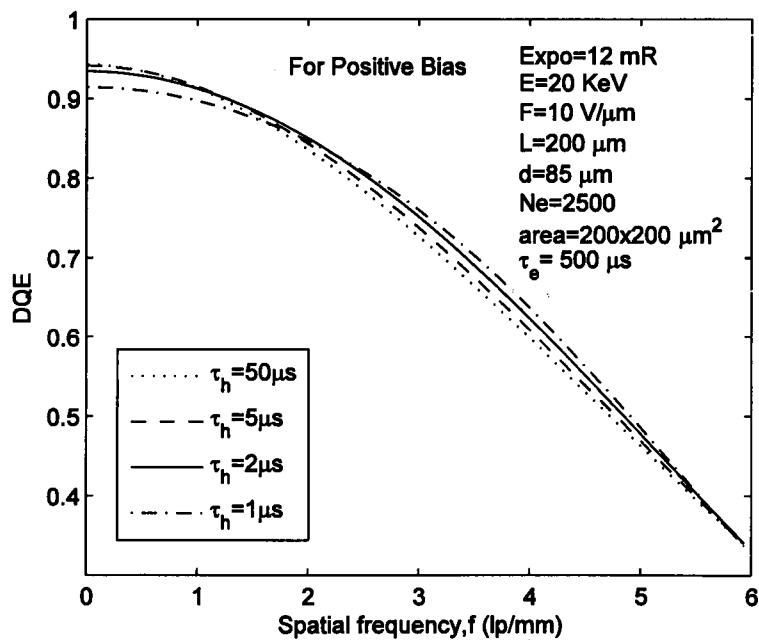
Figure 4.9 The theoretical DQE for mammography in a positively biased a-Se detector. (a) DQE versus spatial frequency for various levels of electron lifetimes (τ_e). (b) DQE versus spatial frequency for various levels of hole lifetimes (τ_h).

The DQE increases with increasing τ_e as shown in Figure 4.9(a). The DQE reaches a plateau when τ_e is approximately 200μs.

Figures 4.10(a) and 4.10(b) show the DQE of negatively biased a-Se detectors as a function of spatial frequency for various levels of electron and hole lifetimes, respectively, for mammographic applications. The a-Se detector is exposed to 12 mR exposure at photon energy of 20 keV (monoenergetic beam). The DQE monotonously decreases with increasing spatial frequency. Both electron's and hole's drift mobilities in a-Se are reasonably well defined so that $\mu\tau$ products depend primarily on the carrier lifetimes [22].

The DQE decreases with decreasing the electron lifetimes and it drops drastically if the electron lifetime is lower than 50 μs as shown in Figure 4.10(a). The DQE remains unchanged if the hole lifetime is higher than 5 μs as shown in Figure 4.10(b). It is evident from figures 4.10(a) and 4.10(b) that the DQE is much more dependent on electron lifetime than hole lifetime for the negative bias. The DQE is more dependent on carrier lifetimes for negative bias than for positive bias.
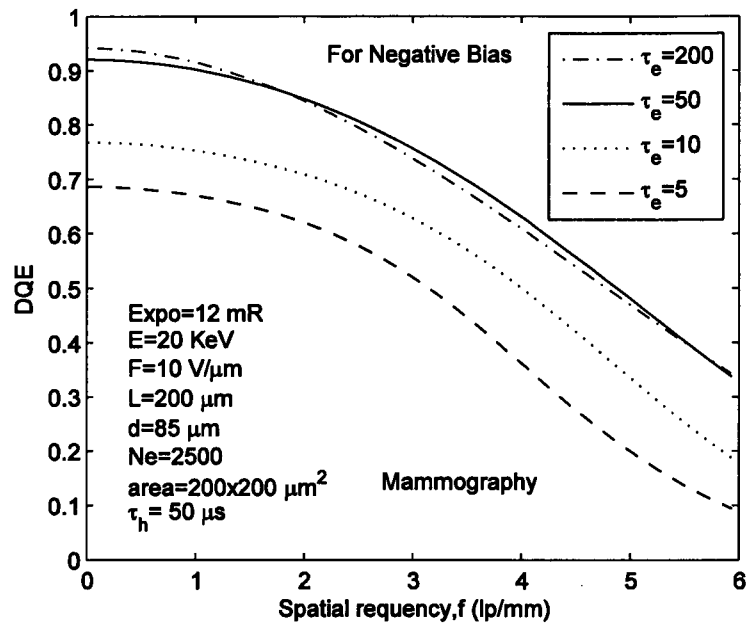
(a)

(b)

Figure 4.10 The theoretical DQE for mammography in a negatively biased a-Se detector. (a) DQE versus spatial frequency for various levels of electron lifetimes (τ_e). (b) DQE versus spatial frequency for various levels of hole lifetimes (τ_h).
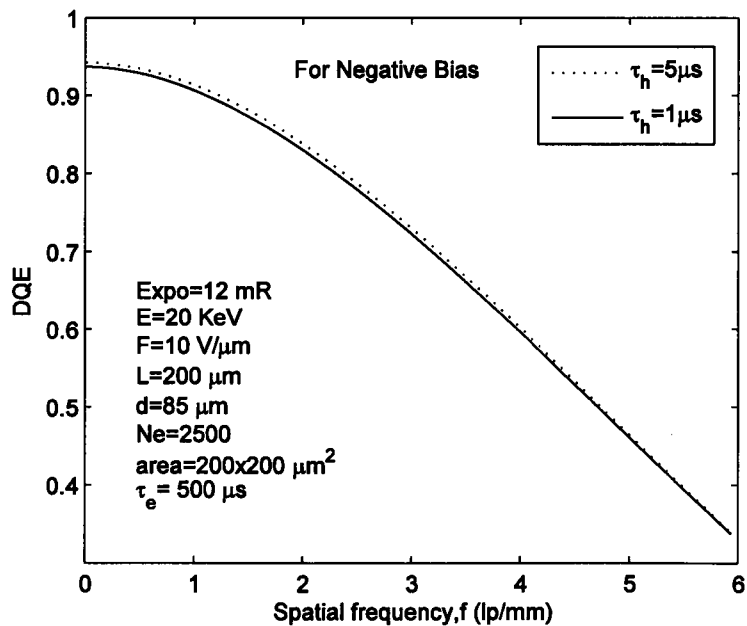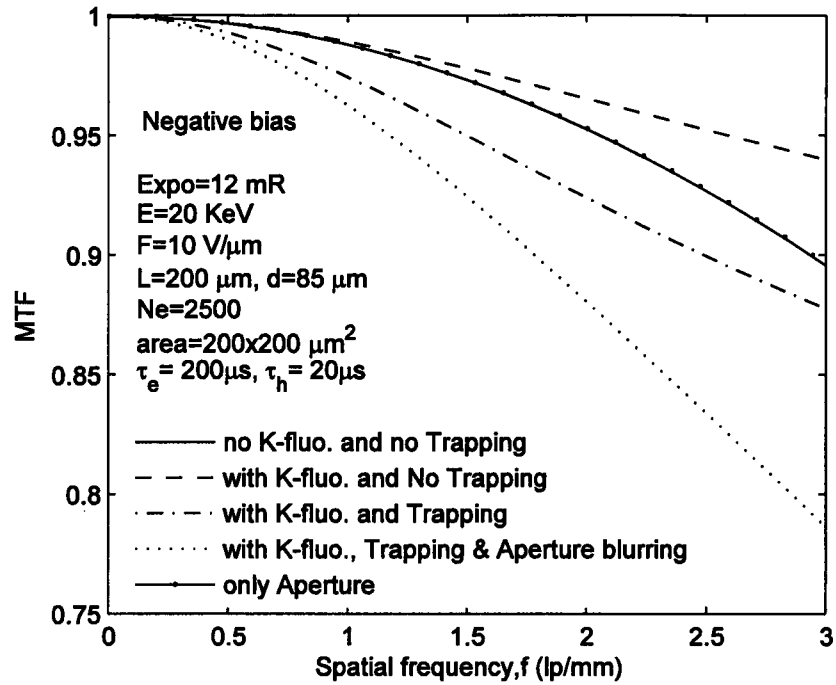
Figure 4.11 MTF versus spatial frequency considering the effects of K-fluorescence, trapping and aperture for mammographic application of a-Se x-ray imaging detector.

The MTFs due to the various scattering mechanism in a-Se detectors for mammographic applications are shown in Figure 4.11. The MTF depends significantly on the carrier trapping and the K-fluorescence reabsorption.

4.5 Model Validation for Mammography
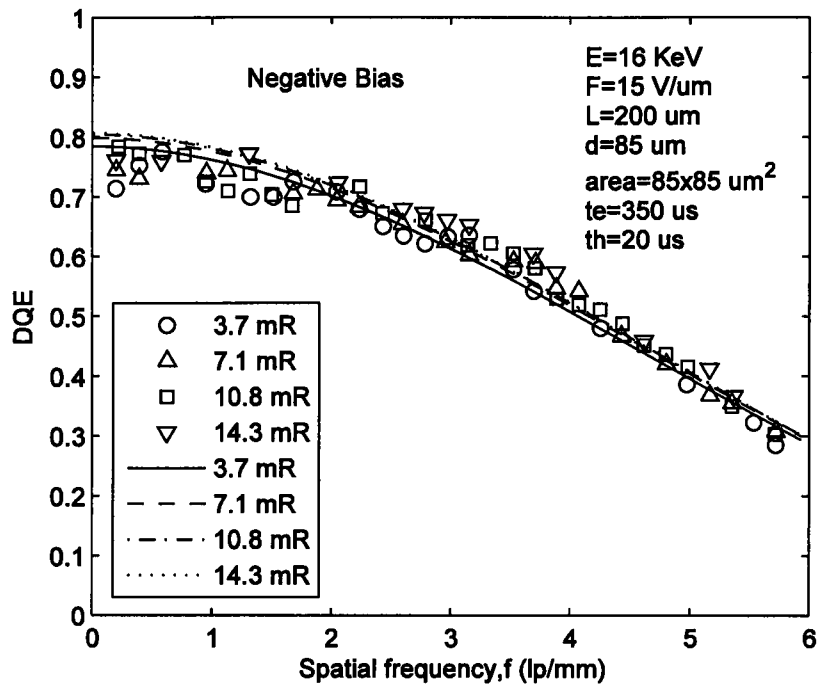
Figure 4.12 Comparison between measured and calculated DQE(f) of the prototype detector: the solid line, dashed line, dashed-dotted line and dotted line are the calculated DQE(f); the scattered data symbols are DQE(f) measurements obtained at different x-ray exposures which are extracted from Fig 12 of Ref [36].

The DQE(f) measurements of an amorphous-Selenium based direct-conversion flat-panel prototype x-ray imaging detector is extracted from the journal paper by Zhao et al.[36] and is shown in Figure 4.12. The circle, triangle and square symbols are representing the experimental data of DQE(f) for different exposure. The solid line, dashed line, dashed-dotted line and dotted lines are representing the DQE(f) which are calculated by the presented model. The detector's thickness is 200 μm, the pixel size is 85 μm, and it is operated with an electric field of 15 V/μm. The incoming x-ray is

produced by using an x-ray tube with a potential of 28 kVp, and with a Molybdenum target and 30-μm-thick Mo and 3.9 cm Lucite filters. The potential applied on the x-ray tube is converted into effective energy, which is 16 keV.

In the figure 4.12, the calculated DQE(f) shows very good agreement with the experimental data. Here, in order to achieve the best fitting result, it is assumed that the electron and hole's life-time are 350 μs and 20 μs, respectively.

4.6 Summary

A parallel cascaded linear system model that includes reabsorption of K-fluorescence x-ray and stochastic blurring due to it and stochastic blurring due to charge carrier trapping has been considered for the calculations of the DQE(f) of a-Se and HgI$_2$ based direct conversion x-ray image detectors. The DQE(f) model can be applied to other potential photoconductive x-ray imaging detectors (poly-CdZnTe, PbI$_2$) considering their practical operating conditions.

CHAPTER 5 CONCLUSION, CONTRIBUTIONS & FUTURE WORK

5.1 Conclusion

DQE(f) is a useful tool for evaluating the overall performance of an x-ray imaging detector. The overall frequency dependent Detective Quantum Efficiency-DQE(f) model of amorphous-Selenium and poly-HgI$_2$ based direct-conversion flat-panel x-ray imaging detector is proposed in this thesis. The overall DQE(f) includes the effects of reabsorption of K-fluorescent x-rays, the range of primary photoelectrons, charge carrier trapping, aperture function, noise aliasing and addition of electronic noise. The derivations, calculations and discussions of each component and the overall DQE(f) are presented, and the simulation results are analyzed and compared with recent published experimental data, which shows a good agreement with the theoretical analysis of the model. The proposed DQE(f) model offers the information to obtain better medical image quality.

Applying this model, the DQE(f) of a-Se and HgI$_2$ based detectors for fluoroscopic and mammographic applications are examined in detail as a function of charge transport parameters under different operating conditions (x-ray exposure, bias voltage, thickness of detector).

It is shown that DQE(f) depends sensitively on the charge transport properties ($\mu\tau'$) of the photoconductors and hence the charge collection efficiency. With the radiation receiving electrode negatively biased, the DQE(f) is much more dependent on electron lifetime than hole lifetime for fluoroscopic and mammographic applications. For mammographic application, the DQE(f) of a-Se detector is higher for positive bias than for negative bias. The results suggest that the DQE can be improved by ensuring that the

carrier with the higher mobility-lifetime product is drifted towards the bottom electrode. There exists an optimum detector thickness that maximizes the DQE under charge carrier trapping. The DQE(f) model is applied to explain experimental DQE data on a-Se and HgI$_2$ based imaging detectors and the model shows a very good agreement with experimental DQE data of fluoroscopic and mammographic applications.

5.2 Contributions

The contribution of this thesis are as follows:

- A theoretical model is developed for calculating DQE(f) by incorporating charge carrier trapping effect in a-Se and poly-HgI$_2$ based direct-conversion flat-panel x-ray imaging detectors.

- The effect of reabsorption of K-fluorescent x-rays is included into the model.

- A theoretical model is developed for calculating DQE(0) considering parallel cascaded system.

- Applying this model on a-Se and HgI$_2$ based detectors, DQE(f) for fluoroscopic and mammographic applications are examined as a function of charge transport parameters under different operating conditions (x-ray exposure, bias voltage, detector thickness).

- Model validations for fluoroscopy and mammography are shown by comparing the theoretical results with the recent published experimental results.

5.3 Suggestions and Future Work

The DQE performance of a-Se and HgI_2 based x-ray imaging detectors is examined in this thesis. There are other photoconductive materials available which have a good prospect to use as an x-ray detector material. There has been an active research on these photoconductive materials so that they could be used to make x-ray imaging detector commercially. The proposed model is not only valid for a-Se or HgI_2 based x-ray imaging detector but it could be applied to find out DQE(f) of other kind of photoconductor materials also. Now-a-days, research is going on with CdZnTe, PbI_2, PbO based photoconductor materials. By changing the parameters (as used for a-Se or HgI_2) in the model according to the new photoconductive material, the same model can be used to obtain the DQE(f) value for the corresponding material. In this way, DQE(f) of different photoconductor based x-ray imaging detector could be determined. As DQE(f) is the measure of the overall performance of an x-ray imaging detector, the photoconductive material which will show the highest DQE(f) could be used to manufacture the x-ray imaging detector considering the other criterion like production cost, availability etc. So, in future, this model can be applied to other direct-conversion flat-panel x-ray imaging detector systems as well.

In the proposed model, the effect of Compton scattering has not considered. The effect of Compton scattering is negligible for the low energy application like mammography or fluoroscopy. But in case of high energy (few MeV) application like x-ray radiation therapy detectors, the effect of Compton scattering could be included in the present model.

REFERENCES

[1] J. A. Rowlands and S. O. Kasap, "Amorphous semiconductors usher in digital x-ray imaging", *Physics Today*, **50**, pp. 24-30, and references therein, 1997.

[2] S. O. Kasap and J. A. Rowlands, "Direct-conversion flat panel X-ray image detectors", *IEE Proc.*,**149**, pp. 85-96, 2002.

[3] B. Polischuk, Z. Shukri, A. Legros, and H. Rougeot, "Selenium direct converter structure for static and dynamic x-ray detection in medical imaging", *Proc. SPIE*, **3336**, pp. 494-504, 1998.

[4] J. A. Rowlands and J. Yorkston, "Flat panel detectors for digital radiography" in Handbook of Medical Imaging Vol. 1, edited by J. Beutel, H. L. Kundel and R. L. Van Metter (SPIE Press, Washington, 2000), Ch. 4 and references therein.

[5] A. R. Cowen, A. G. Davies and M. U. Sivananthan, "The design and imaging characteristics of dynamic, solid-state, flat-panel x-ray image detectors for digital fluoroscopy and fluorography", *Clinical Radiology*, **63**, pp. 1073-1085, 2008.

[6] E. Samei and M. J. Flynn, "An experimental comparison of detector performance for direct and indirect digital radiography systems", *Med. Phys.*, **30**, pp. 608-622, 2003.

[7] R. S. Saunders Jr., E. Samei and C. Hoeschen, "Impact of resolution and noise characteristics of digital radiographic detectors on the detectability of Lung nodules", *Med. Phys.*, **31**, pp. 1603-1613, 2004.

[8] M. Choquette, H. Rougeote, J. Martin, L. Laperriere, Z. Shukri and B. Polischuk, "Direct selenium x-ray detector for fluoroscopy, R&F, and radiography", *Proc. SPIE*, **3977**, pp.128-136, 2002.

[9] B. Polischuk, H. Rougeote, K. Wong, A. Debrie, E. Poliquin, M. Hansrol, J. P. Martin, T. T. Truong, M. Choquette, L. Laperriere and Z. Shukri, "Direct conversion detector for digital for digital mammography", *Proc. SPIE*, **3659**, pp. 417-425, 1999.

[10] B. Zhao and W. Zhao, "Themporal performance of amorphous selenium mammography detectors", *Med. Phys.*, **32**, pp. 128-136, 2005.

[11] Z. Su, L. E. Antonuk, Y. El-Mohri, L. Hu, H. Du, A. Sawant, Y. Li, Y. Wang, J. Yamamoto and Q. Zhao, "Systematic investigation of the signal properties of polycrystalline HgI_2 detectors under mammographic, radiographic, fluoroscopic and radiotherapy irradiation conditions", *Phys Med Biol*, **50**, pp. 2907-2928, 2005.

[12] T. Weitkamp, C. David, O. Bunk, J. Bruder,P. Cloetens and F. Pfeiffer, " X-ray phase radiography and tomography of soft tissue using grating interferometry", *European Journal of Radiology*, **68**, S13–S17, 2008.

[13] M. Overdick, C. Bäumer, K. J. Engel, J. Fink, C. Herrmann, H. Krüger, M. Simon, R. Steadman, and G. Zeitler, "Status of Direct Conversion Detectors for Medical", *IEEE trans. Nuc. Sci.* Vol.**56**, No.4, pp. 1800-1809, 2009.

[14] M. Z. Kabir, S.O. Kasap and J.A. Rowlands, "Photoconductors for x-ray image detectors", in Springer Handbook of Electronic and photonic Materials, (Springer, Würzburg, 2006), Ch. 48.

[15] S. O. Kasap and J. A. Rowlands, "X-ray photoconductors and stabilized a-Se for direct conversion digital flat panel x-ray image detectors", in Optoelectronics & Photonics: Principles and Practices, S.O. Kasap, (Prentice-Hall, Upper Saddle River, New Jersey, 2001).

[16] M. Z. Kabir, E. V. Emelianova, V. I. Arkhipov, M. Yunus, S. O. Kasap, and G. Adriaenssens, "The effect of large signals on charge collection in radiation detectors: Application to amorphous selenium detectors", *J. Phys. D: Appl. Phys.*, **99**, 2006.

[17] R. A. Street, S. E. Ready, K. Van Schuylenbergh, J. Ho, J. B. Boyec, P. Nylen, K. Shah, L.Melekhov, and H. Hermon, "Comparison of PbI_2 and HgI_2 for direct detection active matrix x-ray image sensors", *J. Appl. Phys.*, **91**, pp. 3345-3355, 2002.

[18] J. M. Boone, "X-ray production, interaction, and detection in diagnostic imaging", in Handbook of Medical Imaging, Vol. 1, edited by J. Beutel, H. L. Kundel and R. L. Van Metter (SPIE Press, Washington), chapter 1 and references therein, 2000.

[19] I. M. Blevis, D. C. Hunt and J. A. Rowlands, "Measurement of X-ray photogeneration in amorphous selenium", *J. Appl. Phys.*, **85**, pp. 7958-7963, 1999.

[20] W. Que and J. A. Rowlands, "X-ray imaging using amorphous selenium: Inherent spatial resolution", *Med. Phys.* **22**, pp. 365-374, 1995.

[21] K. Kanaya and S. Okayama, "Penetration and energy-loss theory of electrons in solid targets", *J. Phys.*, **5**, pp. 43-58, 1972.

[22] S. O. Kasap, "X-ray sensitivity of photoconductors: application to stabilized *a*-Se", *J. Phys. D: Appl. Phys.*, **33**, pp. 2853-2865, 2000.

[23] G. Pang, W. Zhao and J.A. Rowlands, "Digital radiology using active matrix readout of amorphous selenium: geometric and effective fill factors", *Med. Phys.* **25**, pp. 1636-1646, 1998.

[24] H. P. Chan and K. Doi, "Energy and angular dependence of x-ray absorption and its effect on radiographic response in screen-film systems", *Phys. Med. Biol.* **28**, pp. 565–579, 1983.

[25] R. K. Swank, "Absorption and noise in x-ray phosphors", *J. Appl. Phys.* **44**, pp. 4199–4203, 1973.

[26] C. E. Metz and C. J. Vyborny, "Wiener spectral effects of spatial correlation between the sites of characteristic x-ray emission and reabsorption in radiographic screen-film systems", *Phys. Med. Biol.* **28**, pp. 547–564, 1983.

[27] I. A. Cunningham, "Linear systems modeling of parallel cascaded stochastic processes: The NPS of radiographic screens with reabsorption of characteristic X radiation", *Proc. SPIE* **3336**, pp. 220–230, 1998.

[28] J. M. Boone, J. A. Seibert, J. M. Sabol and M. Tecotzky, "AMonte Carlo study of x-ray fluorescence in x-ray detectors", *Med. Phys.* **26**, pp. 905–916, 1999.

[29] W. Hillen, W. Eckenbach, P. Quadflieg, and T. Zaengel, "Signal-to-noise performance in cesium iodide x-ray fluorescent screens", Proc. SPIE. **1443**, 120–131, 1991.

[30] W. Zhao, W. G. Ji and J. A. Rowlands, "Effects of characteristic x rays on the noise power spectra and detective quantum efficiency of photoconductive x-ray detectors", *Med. Phys.* **28**, pp. 2039–2049, 2001.

[31] D. R. Dance and G. Y. Day, "Escape probabilities for fluorescent x-rays", *Phys. Med. Biol.* **30**, pp. 259-262, 1985.

[32] S. A. Mahmood, M. Z. Kabir, O. Tousignant, H. Mani, J. Greenspan and P. Botka, "Dark current in multi-layer amorphous selenium X-ray imaging detectors", *Appl. Phys. Lett.* **92**, pp. 223506, 2008.

[33] D. C. Hunt, O. Tousignant and J. A. Rowlands, "Evaluation of the imaging properties of an amorphous selenium-based flat panel detector for digital fluoroscopy", *Med. Phys.* **31**, pp.1166-1175, 2004.

[34] H. Du, L. E. Antonuk, Y. El-Mohri, Q. Zhao, Z. Su, J. Yamamoto and Y. Wang, "Investigation of the signal behavior at diagnostic energies of prototype, direct detection, active matrix, flat-panel imagers incorporating polycrystalline HgI₂ ", *Phys. Med. Biol*, **53**, pp. 1325-1351, 2008.

[35] W. G. Ji, W. Zhao and J. A. Rowlands, "Digital x-ray imaging using amorphous selenium: Reduction of aliasing", *Med. Phys.* **25**, pp. 2148-2162, 1998.

[36] W. Zhao, W. G. Ji, A. Debrie and J. A. Rowlands, "Imaging performance of amorphous selenium based flat-panel detectors for digital mammography: Characterization of a small area prototype detector", *Med. Phys.*, **30**, pp. 254-263, 2003.

[37] M. Zahangir Kabir and S. O. Kasap, "Charge collection and absorption-limited sensitivity of x-ray photoconductors: Applications to a-Se and HgI$_2$", *Appl. Phys. Lett.*, **80**, pp. 1664-1666, 2002.

[38] M. Zahangir Kabir and S. O. Kasap, "DQE of photoconductive x-ray image detectors: application to a-Se", *J. Phys. D: Appl. Phys.*, **35**, pp. 2735-2743, 2002.

[39] M. Rabbani, R. Shaw and R. Van Metter, "Detective quantum efficiency of imaging systems with amplifying and scattering mechanisms", *J. Opt. Soc. Am. A* **4**, pp. 895-901, 1987.

[40] J. G., Mainprize, D. C. Hunt, and M. J. Yaffe, "Direct conversion detectors: the effect of incomplete charge collection on detective quantum efficiency", *Med. Phys.*, **29**, pp. 976-990, 2002.

[41] M. Z. Kabir, "Effects of charge carrier trapping on polycrystalline PbO x-ray imaging detectors", *J. Appl. Phys.*, **104**, pp. 074506-9, 2008.

[42] S. O. Kasap, "Principles of electronic materials and devices", 2nd edition, (McGraw-Hill, New York), chapter 1, 2002.

[43] G. Zentai, L. Partain, R. Pavlyuchkova, C. Proano, B. N. Breen, A. Taieb, O. Dagan, M. Schieber, H. Gilboa, and J. Thomas, "Mercuric iodide medical imagers for low exposure radiography and fluoroscopy", *Proc. SPIE*, **5368**, pp. 200-210, 2004.

[44] M. Schieber, A. Zuck, M. Braiman, J. Nissenbaum, R. Turchetta, W. Dulinski, D. Husson, and J.L. Riester, "Novel mercuric iodide polycrystalline nuclear particle counters", *IEEE trans. Nuc. Sci.* **NS-44**, pp. 2571-2575, 1997.

[45] W. Zhao and J.A. Rowlands, "X-ray imaging using amorphous selenium: Feasibility of a flat panel self-scanned detector for digital radiology", *Med. Phys.* **22**, pp. 1595-1604, 1995.

[46] M. Z. Kabir and S. O. Kasap, "Modulation transfer function of photoconductive x-ray image detectors: effects of charge carrier trapping", *J. Phys. D: Appl. Phys.*, vol. **36**, pp. 2352-2358, 2003.

[47] I. A. Cunningham, in *Handbook of Medical Imaging*, edited by J. Beutel, H. L. Kundel, and R.L. Van Metter, (SPIE Press, Washington, 2000), Vol. 1, Chap. 2.

[48] W. Zhao and J. A. Rowlands, "Digital radiology using active matrix readout of amorphous selenium: theoretical analysis of detective quantum efficiency", *Med. Phys.* **24**, pp. 1819-1833, 1997.

[49] http://physics.nist.gov/PhysRefData/

[50] M. Z. Kabir, **M. W. Rahman** and W. Y. Shen, "Modeling of the DQE(f) of direct conversion x-ray imaging detectors incorporating charge carrier trapping and K-fluorescence", *IEEE trans. Nuc. Sci.* - Submitted.

[51] G. W. C. Kaye and T. H. Laby, "Tables of physical and chemical constants", (Longman, England, 1995), 16th edition.